

AD_____

AWARD NUMBER: W81XWH-05-1-0278

TITLE: Image Processing and Computer Aided Diagnosis in Computed Tomography of the Breast

PRINCIPAL INVESTIGATOR: Jessie Qing Xia, Ph.D.

CONTRACTING ORGANIZATION: Duke University
Durham, North Carolina 27710

REPORT DATE: March 2006

TYPE OF REPORT: Annual Summary

PREPARED FOR: U.S. Army Medical Research and Materiel Command
Fort Detrick, Maryland 21702-5012

DISTRIBUTION STATEMENT: Approved for Public Release;
Distribution Unlimited

The views, opinions and/or findings contained in this report are those of the author(s) and should not be construed as an official Department of the Army position, policy or decision unless so designated by other documentation.

REPORT DOCUMENTATION PAGE				<i>Form Approved</i> OMB No. 0704-0188	
Public reporting burden for this collection of information is estimated to average 1 hour per response, including the time for reviewing instructions, searching existing data sources, gathering and maintaining the data needed, and completing and reviewing this collection of information. Send comments regarding this burden estimate or any other aspect of this collection of information, including suggestions for reducing this burden to Department of Defense, Washington Headquarters Services, Directorate for Information Operations and Reports (0704-0188), 1215 Jefferson Davis Highway, Suite 1204, Arlington, VA 22202-4302. Respondents should be aware that notwithstanding any other provision of law, no person shall be subject to any penalty for failing to comply with a collection of information if it does not display a currently valid OMB control number. PLEASE DO NOT RETURN YOUR FORM TO THE ABOVE ADDRESS.					
1. REPORT DATE (DD-MM-YYYY) 01-03-2006		2. REPORT TYPE Annual Summary		3. DATES COVERED (From - To) 1 Mar 2005 – 28 Feb 2006	
4. TITLE AND SUBTITLE Image Processing and Computer Aided Diagnosis in Computed Tomography of the Breast				5a. CONTRACT NUMBER	
				5b. GRANT NUMBER W81XWH-05-1-0278	
				5c. PROGRAM ELEMENT NUMBER	
6. AUTHOR(S) Jessie Qing Xia, Ph.D. E-Mail: qing.xia@duke.edu				5d. PROJECT NUMBER	
				5e. TASK NUMBER	
				5f. WORK UNIT NUMBER	
7. PERFORMING ORGANIZATION NAME(S) AND ADDRESS(ES) Duke University Durham, North Carolina 27710				8. PERFORMING ORGANIZATION REPORT NUMBER	
9. SPONSORING / MONITORING AGENCY NAME(S) AND ADDRESS(ES) U.S. Army Medical Research and Materiel Command Fort Detrick, Maryland 21702-5012				10. SPONSOR/MONITOR'S ACRONYM(S)	
				11. SPONSOR/MONITOR'S REPORT NUMBER(S)	
12. DISTRIBUTION / AVAILABILITY STATEMENT Approved for Public Release; Distribution Unlimited					
13. SUPPLEMENTARY NOTES					
14. ABSTRACT A novel breast cancer imaging technique – dedicated cone-beam breast CT – is currently under development. It is designed to deliver low dose to a patient while removing the superposition of breast tissues, which is a limiting factor of the conventional mammography technique. The new technique will particularly benefit women with dense breasts. The development of the breast CT imaging technique requires effective and efficient ways to reduce its scattered radiation as well as denoising so as to provide high quality images and help make diagnostic decisions. Therefore, it is important to investigate different possible image processing tools and decide which one is better based on image quality metrics such as contrast-to-noise ratio (CNR) as well as the observer performance study via a receiver operating characteristic (ROC) analysis. The raw breast CT data has been successfully reconstructed via the Feldkamp filtered back projection (FBP) algorithm for cone-beam geometry. A Gaussian noise model taking into account the energy-integrating characteristic of a flat-panel detector has been developed. Based on this model, the maximum likelihood estimate of the scatter free image via the expectation maximization (EM) algorithm has been derived. A partial diffusion equation based image denoising technique has been implemented.					
15. SUBJECT TERMS breast CT, scatter compensation, denoising, breast imaging, CAD, cone-beam CT					
16. SECURITY CLASSIFICATION OF:			17. LIMITATION OF ABSTRACT UU	18. NUMBER OF PAGES 72	19a. NAME OF RESPONSIBLE PERSON USAMRMC
a. REPORT U	b. ABSTRACT U	c. THIS PAGE U			19b. TELEPHONE NUMBER (include area code)

Table of Contents

Introduction.....1

Report Body.....2

Key Research Accomplishments.....5

Reportable outcomes..... 6

Conclusions..... 6

References..... 7

Appendices..... 10

Introduction

1. Clinical Relevance: Breast Cancer

Breast cancer is the most common cancer type that affects women globally [1]. In the United States, due to the long life spans, the incidence is even higher: every one woman over eight will develop breast cancer in her lifetime. It was estimated that approximately 211,240 new invasive breast cancer cases and 58,490 new *in situ* cases would be found in American women in 2005 [2]. Moreover, the disease is the second leading cause of cancer-related death for women in the United States, which was predicted to kill 40,870 women in 2005 [2].

Presently there is no effective way of preventing the disease. However, the detection of the cancer at its early stage has been found to significantly improve the survival rates [3-6]. For example, when the breast cancer is detected at the localized stage, the five year relative survival rate is 98% [2]. By contrast, when it is not found until metastasized, the five year survival rate drops dramatically. In addition, when the cancer is found earlier, more viable treatment options are also available [7-9].

X-ray mammography is a successful tool for the early detection of the breast cancer. The abnormalities can manifest themselves on a mammogram as either masses, clusters of microcalcifications, or architectural distortions even before any symptom shows up. An annual screening program based on mammography is recommended for women older than forty years or younger women with high risk by National Cancer Institute, American Cancer Society and American College of Radiology. It has been proven to reduce the mortality rate of the breast cancer since its initiation. For example, screening mammography decreases the fifteen year mortality for women in their forties by 20% [10]. Also, it is found that screening is most effective for women older than 55 years old [10, 11].

2. Limitation of Screening Mammography

Film-screen X-ray mammography is presently the only FDA approved screening tool aiming at early detection of the breast cancer. While it has been proven to be effective, it is not omnipotent in its detection sensitivity of breast lesions due to several limitations such as two-dimensional (2D) projection data acquisition and restricted range of linear optical response of the detector. Overall, it has a sensitivity within the range of 63% to 88% depending on the patient's age group, family history [12] and breast density [13]. For women with dense breasts, the sensitivity is lower since in their mammograms the dense appearance of the breast tissue is more likely to obscure any abnormalities and makes the detection of breast cancer even more challenging [14]. In addition, the situation gets complicated by the fact that breast density is also a risk factor, which means that women with dense breasts tend to be more likely to get breast cancer.

3. Emerging Dedicated Breast CT Imaging

Breast CT technology offers the potential to detect breast lesions among women with dense breasts, which is a well-known challenging task in conventional film-screen X-ray mammography [15].

The breast imaging via CT modality was first conducted in the late 1970s [16,17]. At that time the breast images were acquired slice-by-slice using x-ray fan-beam geometry. The long scan time, high patient dose together with the limited image quality prevented the further application of this technique.

With the development of flat-panel detectors in recent years, the fast breast imaging via a cone-beam CT became possible and breast CT regained attention. So far, four research groups have fabricated their own dedicated breast CT systems and one research group has set up a virtual breast CT system by applying mathematical models. The four groups with actual breast CT systems are: Dr. Boone's group in University of California, Davis [18,19], Dr. Tornai's group in Duke University [20,21], Dr. Ning's group in University of Rochester [22,23] and Dr. Shaw's group in University of Texas M.D. Anderson Cancer Center [24, 25]. The one group with a virtual breast CT system is Dr. Glick's group in University of Massachusetts [26, 27].

In a conventional CT system, the x-ray tube/ detector move around the torso of a patient; whereas a dedicated breast CT system has a joint x-ray tube/detector move just around the breast. The system is normally set up in the following way: a patient lies supinely on a table with one breast hanging through a hole. The flat-panel detector is installed vertically and moves jointly with the x-ray tube.

By this design of the dedicated system, the field of view (FOV) of the detector can be fully employed for breast imaging. What's more, since no other tissues will attenuate the x-ray beam, the effective glandular dose delivered to the patient can be lowered to match the two-view screening mammograms for the same breast [28].

Although they share the same physical setup, the four breast CT systems differ in their detailed technical aspects: the choice of x-ray beam, the x-ray source orbit, and the peak voltage and tube current values used.

The proposed project is a collaborative effort between our group at Duke and Dr. Boone's group in University of California, Davis. Based on the raw data provided by them, we will develop the techniques for image improvement via the scatter compensation and/or denoising.

Report Body

In the approved statement of work (SOW), it was proposed that *task 1* to *3* would be finished within the first fiscal year. What has been done so far basically follows the SOW with some minor changes, which will be stated in each subsection.

Task 1: Develop and test a unique two-dimensional Bayesian image processing technique on the projection data of cone-beam breast Computed Tomography (breast CT) obtained without a grid.

In the previous work [29], the Bayesian image estimation technique based on Poisson noise model has been successfully applied to reduce the scattering radiation in digital mammograms. While CT projections of the breast are similar enough to give us confidence in its eventual success, this application of BIP is unique and will present novel challenges. For example, in digital mammography, the projection images are the

ultimate images for display and diagnosis; whereas in breast CT, the diagnosis is based on the reconstructed images or its derivatives such as maximum intensity projection (MIP) [30]. To reconstruct the tomographic images, the projection images need to be converted the line integrals of attenuation coefficient via the logarithmic operation. It is expected the characteristics of the noise will be different because of the nonlinear operation. Therefore the component for noise constraining in the BIP, i.e. Gibbs prior, has been modified to incorporate this knowledge.

In addition, while in previous implementations of BIP for digital chest and breast imaging a Poisson noise model was used, the flat-panel detectors actually are integrating detectors and so the Poisson noise model is not exactly correct. A more exact statistical model for the energy-integrating detector has been incorporated into the scatter compensation framework and the maximum likelihood estimate (MLE) of scatter-free image has been acquired via the expectation maximization (EM) algorithm. The details are shown as follows.

1) Signal from an Energy-Integrating Detector

To simplify the notion, assume that the x-ray spectrum impinging on the energy-integrating detector is binned into the discrete energy bands. In our analysis, the primary x-ray photons surviving attenuation and the scattered photons will be analyzed separately, so there are x-ray spectrums for primary and scatter radiations respectively. Moreover, the x-ray spectrums are dependent on the attenuation material and its thickness.

$$n \sim \text{Poisson}(\lambda)$$

$$e = K \sum_{i=1}^n e_i \quad (1)$$

where n is the number of photons hitting on the detector, e_i is the energy carried by individual photon i and follows probability outlined by the x-ray spectrum, K is the gain factor and e is the signal recorded by the energy-integrating detector.

Obviously, the signal e does not follow a Poisson distribution, but rather a compound Poisson distribution [31]. Assuming the first and second central moments of x-ray spectrum for e_i are μ and σ^2 , because of the mutual independence between e_i 's, we get the first and second central moments of e as:

$$E(e) = \bar{e} = E_n(E(K \sum_{i=1}^n e_i | n)) = E_n(K \sum_{i=1}^n E(e_i | n)) = E_n(Kn\mu) = K\lambda\mu, \quad (2)$$

$$\begin{aligned} \text{var}(e) &= \text{var}_n(E(K \sum_{i=1}^n e_i | n)) + E_n(\text{var}(K \sum_{i=1}^n e_i | n)) = \text{var}_n(Kn\mu) + E_n(K^2 n \sigma^2) \\ &= K^2(\lambda\mu^2 + \lambda\sigma^2) = \bar{e} \cdot K \frac{\mu^2 + \sigma^2}{\mu}. \end{aligned} \quad (3)$$

Therefore, a Gaussian approximation of e is:

$$e \sim \text{Gaussian}(\bar{e}, \bar{e} \cdot K \frac{\mu^2 + \sigma^2}{\mu})_+, \quad (4)$$

where $(\cdot)_+$ means that e can only take on the non-negative values.

2) Gaussian noise model

The Gaussian noise model for the scatter radiation is proposed as follows:

$$\begin{aligned} d_i | B, \sigma_{i1}^2 &\sim \text{Gaussian}(b_i, \sigma_{i1}^2) \\ s_i | B, \sigma_{i2}^2 &\sim \text{Gaussian}((B^{**}P)_i, \sigma_{i2}^2) \\ y_i = d_i + s_i | B, \sigma_{i1}^2, \sigma_{i2}^2 &\sim \text{Gaussian}(b_i + (B^{**}P)_i, \sigma_{i1}^2 + \sigma_{i2}^2) \end{aligned}$$

where d_i , s_i , and y_i represent respectively the primary, scatter and total radiations reaching a pixel i . The b_i is the expectation of the primary radiation d_i at pixel i . $B = \{b_i, i=1, \dots, N\}$ is its two-dimensional matrix representation. In addition, σ_{i1}^2 and σ_{i2}^2 represent the variance of the primary radiation and the variance of the scatter radiation in each pixel i .

The EM algorithm for the MLE estimate of B based on the Gaussian noise model is derived via the steps shown in Appendix 2, and the updating equation for b_k at iteration step $n+1$ is:

$$b_k^{(n+1)} = b_k^{(n)} + w_k \cdot [y_k - (b_k^{(n)} + (B^{(n)} ** P)_k)], \quad (5)$$

where

$$w_k = \sigma_{k1}^2 / (\sigma_{k1}^2 + \sigma_{k2}^2). \quad (6)$$

Incorporating the equation (3) into here, we estimate w_k in an iterative manner:

$$\begin{aligned} w_k &= b_k^{(n)} \cdot \frac{\mu_p^2 + \sigma_p^2}{\mu_p} / (b_k^{(n)} \cdot \frac{\mu_p^2 + \sigma_p^2}{\mu_p} + (B^{(n)} ** P)_k \cdot \frac{\mu_s^2 + \sigma_s^2}{\mu_s}) \\ &= b_k^{(n)} / (b_k^{(n)} + (B^{(n)} ** P)_k \cdot (\frac{\mu_s^2 + \sigma_s^2}{\mu_s} / \frac{\mu_p^2 + \sigma_p^2}{\mu_p})) \end{aligned} \quad (7)$$

Other than the existence of a nice analytic formula for b , approximating the sum of energies e by a Gaussian distribution poses an additional advantage: the dark current (dc) and electronic readout noise can be easily incorporated into the framework. The electronic readout noise is usually represented by a Gaussian distribution with variance of σ_{em}^2 . Then both components are jointly modeled by $N(dc, \sigma_{em}^2)$ [32]. Incorporating this into the model shown in equation (4), the signal is now:

$$e \sim \text{Gaussian}(\bar{e} + dc, \bar{e} \cdot K \frac{\mu^2 + \sigma^2}{\mu} + \sigma_{em}^2)_+. \quad (8)$$

Task 2: Reconstruct the three-dimensional breast image based on the processed projection data from Task 1.

An existing ordered subset expectation maximization (OSEM) algorithm for cone-beam CT was configured for tomographic reconstruction. However, there was some severe artifact in the reconstructed volume. The cause of the artifact has not been pinpointed yet. As an alternative, the Feldkamp type filtered back-projection (FBP) algorithm [33] was implemented. Fortunately, due to the sufficient sampling of the projection data and projection views, the FBP algorithm provided good reconstruction results. It is also computationally more efficient than the OSEM algorithm. Therefore, we feel that FBP algorithm is a good substitute for the OSEM algorithm for *Task 2* in the approved SOW.

Task 3: Apply the algorithm in Task 1 to the two-dimensional slices of the reconstructed three-dimensional breast image from the unprocessed projection data.

The BIP algorithm in *Task 1* has been set up primarily for image noise reduction and tried on the reconstructed slice image. Visually, the processed images are smoother than the original ones. Further evaluation will be conducted.

Within the next two fiscal years, *task 4* to *6* will be fulfilled.

Task 4: Develop and test three-dimensional Bayesian image processing technique on the reconstructed image based on the unprocessed projection data acquired without a grid.

Task 5: Develop a Computer Aided Diagnosis tool for detecting breast mass lesions based on the projection data.

Task 6: Test and compare the performances of the CAD developed in Task 5 applied to processed projection data from Task 1 with the CAD performance on the projection data without Bayesian processing.

Due to the limited cases available, a major change to *Task 5* will be an addition of 3D mass simulation routine to generate multiple synthetic datasets as well as simplified ROC analysis. It is felt that this change won't affect the overall structure of the project, since the primary goal of the proposed CAD tool is for the evaluation of the image processing techniques developed during the first two years of the grant.

Key Research Accomplishments

- Proposed a Gaussian noise model for scatter compensation when an energy-integrating detector is used for image acquisition;
- Derived the EM algorithm for the MLE estimate based on the Gaussian noise model;
- Implemented the Feldkamp type FBP for the cone-beam CT;
- Reconstructed the breast CT data;
- Implemented a partial diffusion equation (PDE) based image denoising technique;
- Compare the reconstructed volumes with and without the image processing by the metrics such as CNR;
- Coded the Siddon algorithm for forward projection of 3D voxelized data using cone-beam geometry.

Reportable Outcomes

- The PI finished a project titled ‘Gaussian Noise Model for Scatter Compensation in Digital Mammography’ and earned her Master of Science degree in statistics from Institute of Statistics and Decision Science (ISDS), Duke University. Please refer to Appendix 2.
- The PI applied for the Sally Hughes-Schrader travel grant of Duke University for a potential site visit to the breast CT research group in University of California, Davis in the summer of 2006.

Conclusions

In summary, the development of dedicated cone-beam breast CT imaging technique requires effective and efficient ways to reduce its scattered radiation as well as denoising so as to provide high quality images and help make diagnostic decisions. Therefore, it is important to investigate different possible image processing tools and decide which one is better based on image quality metrics such as CNR as well as the observer performance study via a ROC analysis.

A Gaussian noise model accounting for the energy-integrating characteristic of a flat-panel detector has been developed. Based on this model, the MLE estimate of the scatter free image via the EM algorithm has been derived. A partial diffusion equation based image denoising technique has been implemented.

The raw breast CT data has been successfully reconstructed via the Feldkamp FBP algorithm for cone-beam geometry. The reconstructed images totally eliminate the problem caused by the superposition of breast tissues which is the limitation of the conventional screening mammography.

References

- [1] E. Britannica, "Breast Cancer," *Encyclopedia Britannica*, 2005.
- [2] ACS, "American Cancer Society: Cancer Facts and Figures 2005," *Atlanta, Ga: American Cancer Society*, 2005.
- [3] I. Reiser, R. M. Nishikawa, M. L. Giger, T. Wu, E. Rafferty, R. H. Moore, and D. B. Kopans, "Computerized detection of mass lesions in digital breast tomosynthesis images using two- and three dimensional radial gradient index segmentation," *Technology in Cancer Research & Treatment*, vol. 3 (5), pp. 437-441, 2004.
- [4] C. E. Floyd, Jr, J. Y. Lo, and G. D. Tourassi, "Cased-based reasoning computer algorithm that uses mammographic findings for breast biopsy decisions," *AJR. American Journal of Roentgenology*, vol. 175, pp. 1347-1352, 2000.
- [5] H. P. Chan, J. Wei, B. Sahiner, E. A. Rafferty, T. Wu, M. A. Roubidoux, R. H. Moore, D. B. Kopans, L. M. Hadjiiski, and M. A. Helvie, "Computer-aided detection system for breast masses on digital tomosynthesis mammograms: Preliminary experience," *Radiology*, vol. 238 (1), pp. 1075-1080, 2006.
- [6] V. L. Ernster, J. Barclay, K. Kerlikowske, H. Wilkie, and R. Ballard-Barbash, "Mortality among women with ductal carcinoma in situ of the breast in the population-based surveillance, epidemiology and end results program," *Archives of Internal Medicine*, vol. 160 (7), pp. 953-958, 2000.
- [7] G. Dave, H. Cosmatos, T. Do, K. Lodin, and D. Varshney, "Metaplastic carcinoma of the breast: A retrospective review," *INTERNATIONAL JOURNAL OF RADIATION ONCOLOGY BIOLOGY PHYSICS*, vol. 64 (3), pp. 771-775, 2006.
- [8] R. W. Sahoo S, Jaskowiak N, Tong LP, Heimann R, "Defining negative margins in DCIS patients treated with breast conservation therapy: The University of Chicago experience," *BREAST JOURNAL 11 (4): 242-247 JUL-AUG 2005*, 2005.
- [9] S. Joslyn, "Ductal carcinoma in situ: Trends in geographic, temporal, and demographic patterns of care and survival," *BREAST JOURNAL 12 (1): 20-27 JAN-FEB*, 2006.
- [10] S. W. Fletcher and J. G. Elmore, "Mammographic screening for breast cancer," *New England Journal of Medicine*, vol. 348 (17), pp. 1672-1680, 2003.
- [11] L. Nystrom, I. Andersson, N. Bjurstam, J. Frisell, B. Nordenskjold, and L. E. Rutqvist, "Long-term effects of mammography screening: updated overview of the Swedish randomised trials," *Lancet*, vol. 359 (9310), pp. 909-919, 2002.
- [12] K. Kerlikowske, P. A. Carney, B. Geller, M. T. Mandelson, S. H. Taplin, K. Malvin, V. Ernster, N. Urban, G. Cutter, R. Rosenberg, and R. Ballard-Barbash, "Performance of screening mammography among women with and without a first-degree relative with breast cancer," *Ann Intern Med*, vol. 133 (11), pp. 855-63, 2000.
- [13] T. M. Kolb, J. Lichy, and J. H. Newhouse, "Comparison of the performance of screening mammography, physical examination, and breast US and evaluation of factors that influence them: An analysis of 27,825 patient evaluations," *Radiology*, vol. 225 (1), pp. 165-175, 2002.

- [14] V. P. Jackson, R. E. Hendrick, S. A. Feig, and D. B. Kopans, "Imaging of the Radiographically Dense Breast," *Radiology*, vol. 188 (2), pp. 297-301, 1993.
- [15] R. H. VP Jackson, SA Feig, DB Kopans, "Imaging of the Radiographically Dense Breast," *RADIOLOGY*, vol. 188 (2), pp. 297-301, 1993.
- [16] C. H. J. Chang, J. L. Sibala, F. Lin, W. R. Jewell, and A. W. Templeton, "Preoperative Diagnosis of Potentially Pre-Cancerous Breast Lesions by Computed Tomography Breast Scanner - Preliminary-Study," *Radiology*, vol. 129 (1), pp. 209-210, 1978.
- [17] R. A. McLeod, J. J. Gisvold, D. H. Stephens, J. W. Beabout, and P. F. Sheedy, "Computed Tomography of Soft-Tissues and Breast," *Seminars in Roentgenology*, vol. 13 (3), pp. 267-275, 1978.
- [18] N. T. Boone JM, Lindfors KK, et al., "Dedicated breast CT: Radiation dose and image quality evaluation," *RADIOLOGY*, vol. 221 (3), pp. 657-667, 2001.
- [19] S. N. Boone JM, Nelson TR, "A comprehensive analysis of DgN(CT) coefficients for pendant-geometry cone-beam breast computed tomography," *MED PHYS*, vol. 31 (2), pp. 226-235, 2004.
- [20] R. L. McKinley, M. P. Tornai, E. Samei, and M. L. Bradshaw, "Initial study of quasi-monochromatic X-ray beam performance for X-ray computed mammotomography," *Ieee Transactions on Nuclear Science*, vol. 52 (5), pp. 1243-1250, 2005.
- [21] J. B. Tornai MP, CN Archer, "Feasibility of Application Specific Emission & Transmission Tomography (ASETT) of the breast," *J Nucl Med.*, vol. 43 (5), pp. 39, 2002.
- [22] N. R. Chen B, "Cone-beam volume CT breast imaging: Feasibility study," *MED PHYS*, vol. 29 (5), pp. 755-770, 2002.
- [23] R. Ning, "Flat panel detector-based cone beam volume CT imaging," *MED PHYS*, vol. 30 (6), pp. 1370-1370, 2003.
- [24] C. J. Lai, C. C. Shaw, M. C. Altunbas, Y. Meng, L. Y. Chen, S. J. Tu, T. P. Wang, X. M. Liu, W. T. Yang, and G. J. Whitman, "Effects of radiation dose level on calcification visibility in cone beam breast CT: a preliminary study," *Proceedings of SPIE*, vol. 1642, pp. 164233-1:8, 2006.
- [25] L. Y. Chen, C. C. Shaw, C. J. Lai, M. C. Altunbas, T. P. Wang, S. J. Tu, and X. M. Liu, "Comparison of full-scan and half-scan for cone beam breast CT imaging," *proceedings of SPIE*, vol. 1642, pp. 16424M-1:7, 2006.
- [26] X. Gong, A. A. Vedula, and S. J. Glick, "Microcalcification detection using cone-beam CT mammography with a flat-panel imager," *Physics in Medicine and Biology*, vol. 49 (11), pp. 2183-2195, 2004.
- [27] S. C. Thacker and S. J. Glick, "Normalized glandular dose (DgN) coefficients for flat-panel CT breast imaging," *Physics in Medicine and Biology*, vol. 49 (24), pp. 5433-5444, 2004.
- [28] J. M. Boone, "Breast CT: Its prospect for breast cancer screening and diagnosis," in *2004 Syllabus: Advances in Breast Imaging Physics, Technology, and Clinical Applications*, A. Karellas and M. L. Giger, Eds. Oak Park: ILL: Radiological Society of North America, 2004, pp. 165-177.

- [29] J. Q. Xia, J. Y. Lo, and C. E. Floyd Jr, "Improved SNR in FFDm by replacing the anti-scatter grid with non-linear image processing," *RSNA*, , vol. Chicago ((Abstract)), 2004.
- [30] J. Hsieh, *Computed Tomography: Principle, Design, Artifacts, and Recent Advances*. Bellingham, Washington: SPIE Press, 2002.
- [31] B. R. Whiting, "Signal statistics in x-ray computed tomography," *Proceedings of SPIE*, vol. 4682, pp. 53-60, 2002.
- [32] P. J. La Riviere, "Penalized-likelihood sinogram smoothing for low-dose CT," *Medical Physics*, vol. 32 (6), pp. 1676-1683, 2005.
- [33] L. A. Feldkamp, L. C. Davis, and J. W. Kress, "Practical Cone-Beam Algorithm," *Journal of the Optical Society of America a-Optics Image Science and Vision*, vol. 1 (6), pp. 612-619, 1984.

Appendices

1. List of Abbreviations

BIP	---	Bayesian Image Processing
Breast CT	---	Breast Computed Tomography
CAD	---	Computer Aided Diagnosis
CNR	---	Contrast to Noise Ratio
EM	---	Expectation Maximization
FBP	---	Filtered Back Projection
FDA	---	Food and Drug Administration
FOV	---	Field Of View
MIP	---	Maximum Intensity Projection
MLE	---	Maximum Likelihood Estimator
OSEM	---	Ordered Subset Expectation Maximization
PDE	---	Partial Diffusion Equation
ROC	---	Receiver Operating Characteristic
2D	---	Two-dimensional
3D	---	Three-dimensional

2. Master's Thesis

GAUSSIAN NOISE MODEL FOR SCATTER COMPENSATION IN DIGITAL MAMMOGRAPHY

by

Qing Xia

**Institute of Statistics and Decision Science
Duke University**

Date: _____

Approved:

Michael L. Lavine, Ph.D, Supervisor

Feng Liang, Ph.D

Leslie M. Collins, Ph.D

**A thesis submitted in partial fulfillment of
the requirements for the degree of Master of Science
in the Institute of Statistics and Decision Science
in the Graduate School
of Duke University**

2006

Abstract

Breast cancer is the most common cancer type that affects women worldwide. In the United States, every one woman over eight will develop breast cancer in her lifetime. Although no effective way of preventing the disease has been found, early detection of the cancer through noninvasive breast imaging is desirable because it warrants more choices of viable treatments and higher survival rates. Digital Mammography is among such imaging techniques.

Compton scattering of x-ray photons is one mechanism of attenuating the x-ray beam, which in turn forms the contrast in a projection image. However, its detection in the projection image is a cause of image quality degradation since it will add noise to the image and reduce the contrast. Therefore many efforts are made to reduce the detected scatter radiation in the projection image either by applying some hardware during acquisition or by using post-acquisition software compensation. The method presented in this thesis belongs to the latter category. A Gaussian noise model for scatter is proposed and its EM ML estimation is derived. In addition, Bayesian MAP estimation is obtained by applying a Gibbs prior with a discontinuity adaptive potential function.

The previously proposed Poisson noise model is flawed in that the radiation does not directly follow a Poisson distribution. Instead, a Gaussian distribution can reasonably describe the radiation data. When a computation method like Gibbs

sampling is used, Poisson noise model will give erroneous results due to the incorrect modeling. The conversion factor between radiation and the number of photons is energy dependent. If it is approximated by a constant independent of energy, then the Poisson noise model can be justified through a latent data augmentation scheme when EM algorithm is used.

The reason we pursue the EM computation in this thesis is that it has a nice analytic formula. Due to the large number of pixels in an image and the existence of a convolution operation, the computation can be greatly reduced with this analytic formula.

The digital mammography image of a uniform breast phantom is processed by the MLE and MAP algorithms of Poisson model and Gaussian model. The results are compared through the image quality metrics like the residual scatter radiation, the contrast-to-noise ratio and the spatial resolution.

From the results we get, it is shown that Gaussian noise model can be used to reduce the scatter radiation in the digital mammography images. Its performance is improved by incorporating Gibbs priors without loss of resolution. In addition, Gaussian noise model works slightly better in improving the contrast-to-noise ratio than the Poisson noise model.

Table of Contents

Abstract	ii
List of Tables	vi
List of Figures	vii
List of Abbreviations	x
Acknowledgments	xi
Chapter 1 Introduction	1
1.1 Digital Mammography	1
1.2 Scatter Radiation and Its Degrading Effect on the Quality of Medical Images	3
1.3 Scatter Compensation	6
1.4 Overview of the Thesis	9
Chapter 2 Materials and Methods	11
2.1 Scatter Kernel	11
2.2 Poisson Noise Model	12
2.3 Gaussian Noise Model	13
2.4 Incorporation of Gibbs prior	18
2.5 Image Acquisition	19
2.6 Image Analysis Metrics	20
2.6.1 RSF	21

2.6.2	Contrast, Noise and CNR	21
2.6.3	Resolution	22
Chapter 3	Results and Discussion	24
3.1	Normality Check of the Data	24
3.2	Latent Data Augmentation Scheme for Poisson Model	28
3.3	Comparison between the Two Models	29
3.4	Further Evaluation of Gaussian Noise Model	34
3.4.1	Effect of the Magnitude of the Scatter Kernel	34
3.4.2	Effect of the Delta in the Gibbs prior	38
Chapter 4	Conclusion	43
	References	45

List of Tables

3.1: The resolution results for Poisson model and Gaussian model when delta=0.1.	33
3.2: The resolution results for the Gaussian noise model with different magnitudes of scatter kernel.	38
3.3: The resolution results for Poisson model and Gaussian model when delta=0.2.	40
3.4: The resolution results for Poisson model and Gaussian model when delta=0.05.	42

List of Figures

1.1: Typical energy spectrum of an x-ray beam.	3
1.2: Illustration of possible interactions between x-ray photons and the object to be imaged within the diagnostic x-ray energy range.	5
1.3: A simple example to see the adverse effect of detected scatter radiation on image quality.	6
1.4: An anti-scatter grid can be added on top of the detector to remove scatter radiation.	7
2.1: The three-dimensional surface plot of a scatter kernel with magnitude of 1 and FWHM of 80 pixels.	12
2.2: A sample breast phantom image taken with the beam stop array superimposed.	20
3.1: The histogram of data from a uniform region-of-interest with total of 201x201 pixels in an image acquired with an anti-scatter grid.	25
3.2: The quantile-quantile plot of the same data as in Figure 3.1 with respect to the standard Gaussian distribution with mean of 0 and standard deviation of 1.	26
3.3: One-dimensional profile through the center of a beam stop(or lead	

disc).	26
3.4: The histogram of data from a region-of-interest with total of 441 pixels behind a beam stop in an image acquired without an anti-scatter grid.	27
3.5: The quantile-quantile plot of the same data as in Figure 3.4 with respect to the standard Gaussian distribution with mean of 0 and standard deviation of 1.	27
3.6: RSF vs. iteration plots for MLE and MAP estimator of b from both the Poisson noise model and the Gaussian noise model.	30
3.7: The noise vs. iteration plots for MLE and MAP estimator of b from both the Poisson noise model and the Gaussian noise model.	32
3.8: The contrast noise vs. iteration plots for MLE and MAP estimator of b from both the Poisson noise model and the Gaussian noise model.	32
3.9: The CNR vs. iteration plots for MLE and MAP estimator of b from both the Poisson noise model and the Gaussian noise model.	33
3.10: The RSF vs. iteration curves for the magnitude (M) of the scatter kernel ranging from 0.0 to 0.65.	35
3.11: The noise vs. iteration curves for M ranging from 0.0 to 0.65.	36
3.12: The contrast vs. iteration curves for M ranging from 0.0 to 0.65.	37
3.13: The CNR vs. iteration curves for M ranging from 0.0 to 0.65.	37
3.14: The noise vs. iteration plots for MLE and MAP estimators based on δ of 0.2.	39

3.15: The CNR vs. iteration plots for MLE and MAP estimators based on delta of 0.2.	40
3.16: The noise vs. iteration plots for MLE and MAP estimators based on delta of 0.05.	41
3.17: The CNR vs. iteration plots for MLE and MAP estimators based on delta of 0.05	42

List of Abbreviations

Abbreviation	Expansion
CIF	Contrast Improvement Factor
CNR	Contrast-to-Noise Ratio
MAP	Maximum <i>a posteriori</i> Estimate
MLE	Maximum Likelihood Estimate
ROI	Region of Interest
RSF	Residual Scatter Fraction
SF	Scatter Fraction
SPR	Scatter to Primary Ratio

Acknowledgments

I would like to thank my thesis advisor, Professor Michael L. Lavine, for his great guidance, support and encouragement.

My gratitude also goes to Professor Feng Liang and Professor Leslie Collins for serving on my thesis committee.

My PhD advisor Professor Carey E. Floyd, Jr has offered me the opportunity to work on this project as well as the freedom to explore the new method, for which I am very grateful.

Lastly, I am thankful for the support from my family including my lovely five-month old son. Their love and trust make the experience during the writing of this thesis a memorable one.

Chapter 1

Introduction

1.1 Digital Mammography

Breast cancer is the most common cancer type that affects women worldwide [1]. In the United States, every one woman over eight will develop breast cancer in her lifetime. And it was estimated that approximately 211,240 new cases of invasive breast cancer would be found in American women and the disease would kill 40,410 women in 2005 [2]. Although there is no effective way of preventing the disease, it is desirable to find early signs of the cancer (e.g., impalpable masses and/or micro-calcifications) through noninvasive breast imaging techniques such as x-ray mammography. The detection of the cancer at its early stage warrants more choices of viable treatments and higher survival rates[3-5].

An x-ray mammography system is typically comprised of two major parts: the x-ray source and the detector. Depending on the type of the detector, the mammography system can be either analog or digital. The analog system utilizes a screen-film as the detector, and is the only FDA approved screening tool aiming at the early detection of the breast cancer for women more than 40 years old. While it has been proven to be effective, it has several shortcomings: 1) the analog film has narrow latitude. Overexposure or underexposure of the film will result in a poor

image which will be unacceptable for breast cancer detection and diagnosis. 2) The film development is critical for the quality of the mammogram as well as time-consuming. 3) The radiology department needs a lot of space and personnel to keep the films. And 4) the transfer of the films between departments or hospitals not only is a lot of hassle, but also causes the wear and tear of films, which is inevitable since they are often the only copies of the case. Due to these limitations of using films as the recording media, many radiology departments are trying to go film-less. It is realized by the digital mammography technique.

A digital mammography system utilizes a flat-panel detector instead of a screen-film detector. Recent studies show that the diagnostic accuracy based on digital mammograms is comparable to those based on conventional film mammograms [6, 7]. In some situations, the digital mammography works even better [6]. In addition, a digital mammography system enjoys the following merits. After x-ray exposure, a digital image of the breast can be readily read out from the flat-panel detector within seconds. There is no overexposure or underexposure issue related with this type of image since the flat-panel detectors have a wide latitude and excellent linear relationship between pixel values and exposure levels. The image can be saved into different media. The transfer and copy of the images are easy, fast and reliable. A very recent study [8] shows that the digital mammography images can be accurately transferred via the broadband internet, which will greatly alleviate the problem related to the shortage of mammographers as well as improve the accuracy of the diagnosis. Moreover, the digital format of images makes advanced imaging

(e.g., breast tomosynthesis [9, 10]) and image processing techniques (such as the technique presented in the thesis) feasible.

1.2 Scatter Radiation and Its Degrading Effect on the Quality of Medical Images

X-ray source emits x-ray photons with different energies. Figure 1.1 shows a

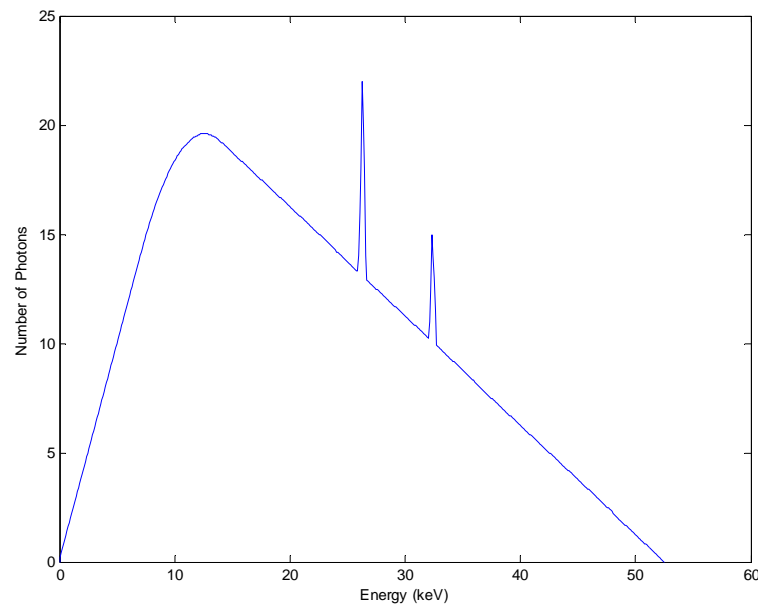


Figure 1.1: Typical energy spectrum of an x-ray beam. The abscissa represents the energy levels that a photon can possibly take on, and ordinate represents the number of photons having the corresponding energy level. The peak voltage (in the unit of kVp) corresponds to maximal energy level. The spectrum shown here has a peak voltage of 52.5 kVp.

typical energy spectrum of an x-ray beam. When the beam passes through the object to be imaged such as a breast, it interacts with the matter and gets attenuated. At the

diagnostic energy level, there are three basic mechanisms for x-ray attenuation: photoelectric effect, Compton scattering and Raleigh scattering [11]. Raleigh scattering, also called coherent scattering, accounts for less than 5% of the total interactions between x-rays and the matter. Therefore it is often omitted for consideration. Photoelectric effect occurs when x-ray photons are totally absorbed by the atoms within the tissue, as illustrated by ray 1 in Figure 1.2. Compton scattering occurs when the photons are deflected from their incident path with partial energy loss. These photons are called scattered photons or scatter radiation, as shown by ray 2 in Figure 1.2. The rest will survive the attenuation and are called the primary photons or primary radiation (ray 3 in Figure 1.2). The primary radiation differs from location to location, which forms the contrast of various tissues in the final image.

The scatter radiation escaped from the imaged object can either miss the detector or impinge on it. The latter will be inevitably detected due to the fact that the detector typically has broad energy sensitivity and does not effectively reject photons that have lost energy by scattering. The total radiation detected is thus the sum of the primary radiation and the scatter radiation. The detection of scattered photons in locations that are different from their original path will add a component of noise and cause the blurring of the image.

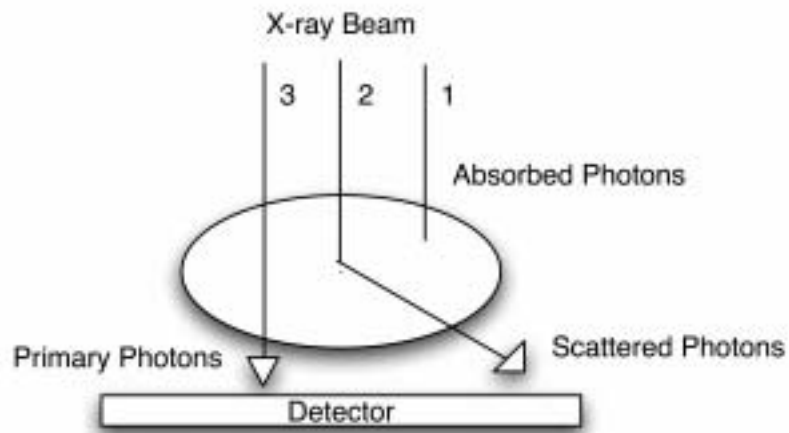


Figure 1.2: Illustration of possible interactions between x-ray photons and the matter within the diagnostic x-ray energy range. The ellipsoid represents the object to be imaged. Photons can be totally absorbed by the photoelectric effect (ray 1), or be scattered through Compton scattering (ray 2) and Raleigh scattering (a very small portion, thus neglected). The rest will survive the attenuation and are called the primary photons or primary radiation (ray 3).

To see how detected scatter radiation adversely affect the quality of a medical image, let's take a look at the simple example shown in Figure 1.3. An ellipsoid lesion is embedded in a uniform background. In the ideal case where no scatter radiation is detected, the total radiation is equal to the primary radiation. In Figure 1.3 (a), assume radiation in the background is P_0 and radiation in the lesion is P_1 , then the contrast of the lesion is $C_1 = (P_1 - P_0) / P_0$. If in practice, a constant scatter radiation S is added all over the image (shown in Figure 1.3(b)), then the radiation in the background becomes $T_0 = P_0 + S$ and radiation in the lesion becomes $T_1 = P_1 + S$. The contrast of the lesion in this image will be $C_2 = (T_1 - T_0) / T_0 = (P_1 - P_0) / (P_0 + S) = C_1 * [P_0 / (P_0 + S)]$, which is smaller than C_1 . That is, the detection of scatter radiation reduces the contrast of the lesion. In cases where scatter is large, lesions can even be

obscured.

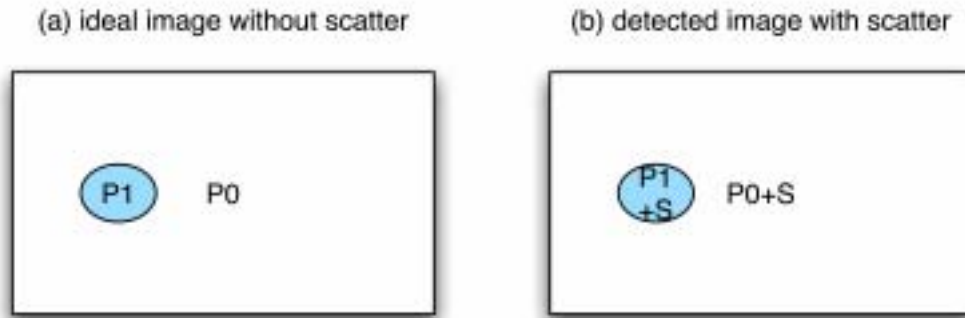


Figure 1.3: A simple example to demonstrate the adverse effect of detected scatter radiation on image quality. An ellipsoid lesion is embedded in a uniform background. (a) The ideal image without scatter radiation is shown. (b) The actual image is shown, which is the sum of primary radiation and scatter radiation. The contrast of the lesion is decreased.

1.3 Scatter Compensation

In summary, the scatter radiation is a physical phenomenon, which together with photoelectric effect causes the attenuation of the x-ray beam. The detection of scatter radiation on the detector will degrade the quality of the image and thus adversely affect the medical diagnosis. This issue exists widely in many imaging techniques such as Single Photon Emission Computed Tomography (SPECT) [12], Positron Emission Tomography (PET) [13], and projection radiographies like chest radiography [14] and mammography [15]. Therefore, it is important to reduce the scatter radiation that is detected. Or in other words, scatter radiation needs to be compensated.

There are two general categories of scatter radiation compensation methods: one

is hardware compensation such as the application of anti-scatter grids [16], slot scanning systems [17], or air gaps [18]; the other is software compensation via post-acquisition image processing, such as simple estimation-subtraction [19], convolution-subtraction [20], de-convolution [21], artificial neural networks [22], maximum likelihood expectation maximization (EM-MLE) [23], or Bayesian image estimation [24, 25].

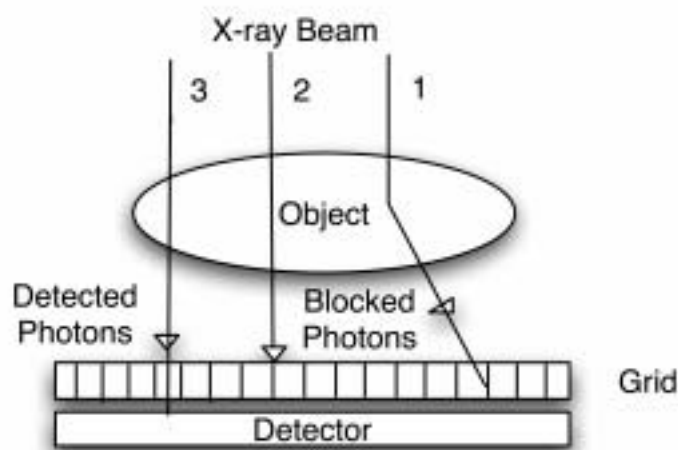


Figure 1.4: An anti-scatter grid can be added on top of the detector to remove scatter radiation. However, as shown by the middle ray, some primary radiation will be blocked as well. To maintain the image quality, the patient dose has to be increased.

An anti-scatter grid is routinely used on a clinical screen-film mammography system. Figure 1.4 illustrates how an anti-scatter grid can be used to reduce the scatter radiation. The orientation of the grid slots is parallel to the primary radiation. Most primary radiation will pass through the slots and reach the detector. Scatter radiation, by contrast, will mostly hit on the metal slits and be absorbed by them.

Thus an anti-scatter grid effectively removes many scatter radiation. Its major drawback is that it also removes some primary radiation, as shown by the middle ray of Figure 1.4. To maintain the same image quality, the magnitude of the x-ray beam needs to be increased, which will also increase the total absorbed dose of the patient.

By contrast, post-acquisition image processing techniques won't change the dose that a patient receives. In addition, some studies [15, 24] show that they can be more effective than an anti-scatter grid in scatter compensation.

A fundamental assumption behind the image processing techniques is that the scatter radiation can be approximated by the convolution of the primary radiation and a scatter kernel. It is verified both theoretically [26] and empirically [27, 28]. In the two-dimensional case, if Y is used to represent the matrix of detected total radiation at each pixel, D for the matrix of the primary radiation, S for the matrix of the scatter radiation, and P for the matrix of the scatter kernel, then the following equation is true:

$$Y = D + S = D + D ** P = D ** (\delta + P), \quad (1.1)$$

where $**$ is the two-dimensional convolution operator and δ is the Dirac delta function in a matrix form. The task of scatter compensation is equivalent to estimating the unknown D from the measured Y .

One solution is to de-convolve the Equation (1.1) [21, 29, 30]. If this is done through the Fourier Transform (FT), then

$$D = FT^{-1}\left(\frac{FT(Y)}{FT(\delta + P)}\right). \quad (1.2)$$

Or, statistical models can be formulated to solve the problem. In the past Poisson noise model was used, which assumed that both primary radiation and scatter radiation follow Poisson distributions. The maximum likelihood estimate (MLE) of D in two-dimensional projection radiography was obtained by borrowing the iterative equation originally derived for SPECT reconstruction [23], and it was combined with a Gibbs prior to form the maximum *a posteriori* (MAP) estimator of D [24]. Later a revision was made on the iterative equation [26]. Although promising, the Poisson noise model presents some problems: 1) the primary radiation and scatter radiation can not be directly modeled to follow Poisson distribution; 2) due to the polychromatic characteristic of x-ray beam, the radiation is not only related to the number of photons but to the energies of the photons as well. Therefore, in this thesis, a new explanation is given that justifies the Poisson noise model, and a new model is proposed, implemented and tested on the digital mammography data for the reduction of detected scatter radiation.

1.4 Overview of the Thesis

The thesis is organized as follows. In Chapter 2, the old Poisson noise model is briefly introduced. The Gaussian noise model is then proposed and its analytical EM algorithm is derived. Moreover, the Gibbs prior is incorporated into the algorithm to constrain the noise in the processed image. Chapter 3 presents the latent data augmentation scheme to justify the Poisson noise model, the image processing

results obtained from both the Poisson model and the Gaussian model, their comparison as well as the some further evaluation of the Gaussian noise model. The thesis is concluded in chapter 5.

Chapter 2

Materials and Methods

2.1 Scatter Kernel

Towards the end of the previous chapter, we mentioned that scatter radiation is often modeled as the convolution of the primary radiation and a scatter kernel. The scatter kernel is also called scatter point spread function (PSF). Experiments [31, 32] and Monte-Carlo simulation models [33, 34] showed that the scatter kernel can be represented by a circularly symmetric exponential decay curve. The curve can be uniquely determined by two parameters: the magnitude (M) and full width at half maximum (FWHM). The two parameters are illustrated in Figure 2.1 (a). Figure 2.1(b) shows the three-dimensional representation of such a scatter kernel with M of 1 and FWHM of 80 pixels. Throughout the thesis, matrix P is used to represent the scatter kernel and it is known *a priori*.

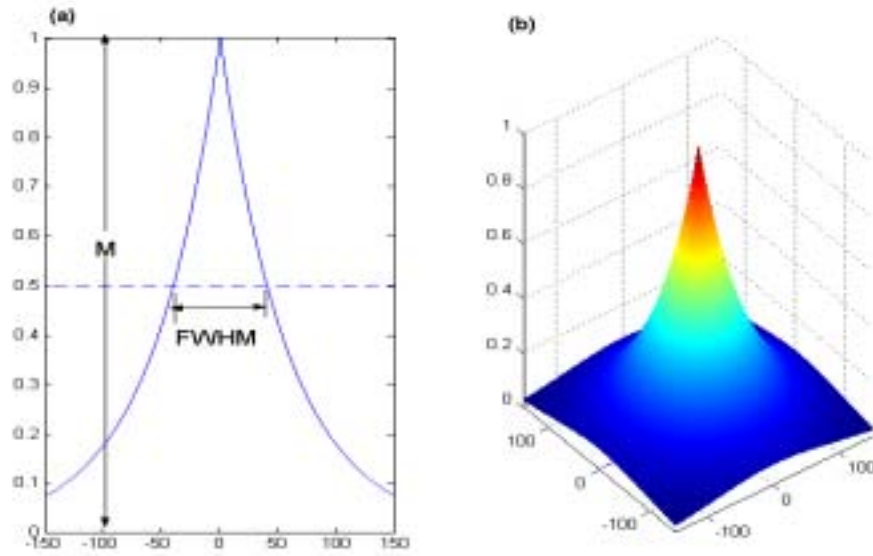


Figure 2.1: A sample scatter kernel with magnitude of 1 and FWHM of 80 pixels. (a) One-dimensional profile of the kernel. (b) Its three-dimensional surface plot.

2.2 Poisson Noise Model

When put in a statistical framework, equation (1.1) becomes:

$$E(Y) = E(D + S) = B + B ** P, \quad (2.1)$$

where $B = E(D)$. If we use d_i , s_i , and y_i ($i=1, \dots, N$; N is the total number of pixels in the image) to represent the elements in the matrices D , S and Y , then Poisson noise model is as follows:

$$\left[\begin{array}{l} d_i | B \sim \text{Poisson}(b_i) \\ s_i | B \sim \text{Poisson}((B ** P)_i) \\ y_i = d_i + s_i | B \sim \text{Poisson}(b_i + (B ** P)_i) \end{array} \right], \quad (2.2)$$

where d_i and s_i ($i=1, \dots, N$) given B are mutually independent. The purpose of using

$(B^{**}P)_i$ to represent $\sum_{j=1}^N b_j p_{ij}$ is two-folds: 1) $(B^{**}P)_i$ is more straightforward than

$\sum_{j=1}^N b_j p_{ij}$ and 2) it is a reminder to us that two-dimensional convolution has a fast

implementation in Fourier domain. We are interested in estimating $B = \{b_i ; i=1, \dots, N\}$.

In [26], a detailed derivation of MLE estimators of B through Expectation Maximization was provided. For conciseness, only the final iterative equation is shown here:

$$b_k^{(n+1)} = b_k^{(n)} \cdot \frac{y_k}{b_k^{(n)} + (B^{(n)} ** P)_k} \quad (2.3)$$

2.3 Gaussian Noise Model

The radiation is intrinsically related to the number of photons via a conversion factor, which is a function of the photon energy. Even if an ideal monochromatic x-ray beam is available, i.e. all the photons from the x-ray source carry the same energy, the detected primary photons have the same energy but the detected scatter photons vary in their energy levels, thus causing different radiation or exposure conversion efficiency. This issue will be even more apparent when in practice a polychromatic x-ray beam as what's shown in Figure 1.1 is usually used. In this case even the primary photons will take on different energy levels. The radiation or exposure will be related not only to the number of photons, but also to their individual energies and

the energy-dependent conversion factors.

As will be discussed in the next chapter, our experimental data show that primary d_i and scatter radiation s_i can not be directly modeled as Poisson distribution. By contrast, the data approximately follow Gaussian distribution. Thus, a Gaussian noise model is proposed as follows:

$$\begin{aligned} d_i | B, \sigma_{i1}^2 &\sim \text{Gaussian}(b_i, \sigma_{i1}^2) \\ s_i | B, \sigma_{i2}^2 &\sim \text{Gaussian}((B ** P)_i, \sigma_{i2}^2) \\ y_i = d_i + s_i | B, \sigma_{i1}^2, \sigma_{i2}^2 &\sim \text{Gaussian}(b_i + (B ** P)_i, \sigma_{i1}^2 + \sigma_{i2}^2) \end{aligned} \quad (2.4)$$

where d_i , s_i , y_i and b_i have the same meaning as those in Poisson noise model (in block (2.2)). In addition, σ_{i1}^2 and σ_{i2}^2 represent the variance of the primary radiation and the variance of the scatter radiation in each pixel i .

Due to the convolution operation, the estimation of $B = \{b_i; i=1, \dots, N\}$ directly from Y does not have a simple analytic form. The MLE of B is thus derived through the EM algorithm as follows.

Treat the measured $Y = \{y_i, i=1, \dots, N\}$ as an incomplete dataset, and unobserved $(D, S) = \{(d_i, s_i), i=1, \dots, N\}$ as a complete dataset. The d_i 's and s_i 's given B are mutually independent, therefore the complete data likelihood is:

$$p_c(D, S | B, \{\sigma_{i1}^2, \sigma_{i2}^2; i=1, \dots, N\}) = \prod_{j=1}^N \left[\frac{1}{\sqrt{2\pi\sigma_{j1}^2}} e^{-(d_j - b_j)^2 / 2\sigma_{j1}^2} \cdot \frac{1}{\sqrt{2\pi\sigma_{j2}^2}} e^{-(s_j - (b ** p)_j)^2 / 2\sigma_{j2}^2} \right]. \quad (2.5)$$

Assuming $\{\sigma_{i1}^2, \sigma_{i2}^2; i=1, \dots, N\}$ are known, we will get the complete data log likelihood by taking the logarithm on both sides,

$$L_c(B | D, S) = \sum_{j=1}^N [-(d_j - b_j)^2 / 2\sigma_{j1}^2 - (s_j - (b^{**}P)_j)^2 / 2\sigma_{j2}^2 - \log \sqrt{2\pi\sigma_{j1}^2} - \log \sqrt{2\pi\sigma_{j2}^2}] \cdot \quad (2.6)$$

The EM algorithm is comprised of two steps: one is the E-step where the expectation of the complete data log likelihood with respect to the present estimate of B is computed; and the other is the M-step where a new estimate of B is obtained which will maximize the computed expectation in the E-step.

Firstly, let us consider the E-step:

$$\begin{aligned} Q(B | B^{(n)}) &= E[L_c(B | D, S) | Y, B^{(n)}] \\ &= \sum_{j=1}^N \{ -(b_j^2 - 2d_j^{(n)}b_j) / 2\sigma_{j1}^2 - [(B^{**}P)_j]^2 - 2s_j^{(n)}(B^{**}P)_j \} / 2\sigma_{j2}^2 \\ &\quad + \text{terms independent of } B, \end{aligned} \quad (2.7)$$

$$\begin{aligned} \text{where } d_j^{(n)} &= E[d_j | Y, B^{(n)}] \\ s_j^{(n)} &= E[s_j | Y, B^{(n)}] \end{aligned} \quad (2.8)$$

Secondly, consider the M-step to find $B^{(n+1)}$ that will maximize $Q(B | B^{(n)})$:

$$\frac{\partial Q(B | B^{(n)})}{\partial b_k} = 0 = -(2b_k - 2d_k^{(n)}) / 2\sigma_{k1}^2 - \sum_{j=1}^N [2(B^{**}P)_j p_{jk} - 2s_j^{(n)} p_{jk}] / 2\sigma_{j2}^2.$$

Solving the above equation for b_k gives

$$b_k^{(n+1)} = d_k^{(n)} - \sigma_{k1}^2 \sum_{j=1}^N p_{jk} \cdot [(B^{(n+1)} ** P)_j - s_j^{(n)}] / \sigma_{j2}^2. \quad (2.9)$$

Using $B^{(n)}$ to approximate $B^{(n+1)}$ in the right hand side, we get:

$$b_k^{(n+1)} = d_k^{(n)} - \sigma_{k1}^2 \sum_{j=1}^N p_{jk} \cdot [(B^{(n)} ** P)_j - s_j^{(n)}] / \sigma_{j2}^2. \quad (2.10)$$

As a good estimate of the primary image is formed, $(B^{(n)} ** P)_j - s_j^{(n)} \approx 0$, then,

$$b_k^{(n+1)} \cong d_k^{(n)}. \quad (2.11)$$

The same apparent form was obtained for Poisson noise model in [26]. But due to the different statistical models, the actual forms of $d_k^{(n)}$ are different and so do the iterative formula of b_k . We will get the iterative formula of b_k for the Gaussian noise model through the following theorem.

Theorem 2.1 Let $X \sim \text{Gaussian}(\mu_x, \sigma_x^2)$, $Y \sim \text{Gaussian}(\mu_y, \sigma_y^2)$, independent. Let $Z=X+Y$ be the third random variable. We know that Z follows a Gaussian distribution with mean of $\mu_z = (\mu_x + \mu_y)$ and variance of $\sigma_z^2 = (\sigma_x^2 + \sigma_y^2)$. It can be proved that the conditional distribution of $X|X+Y$ i.e. $X|Z$ is

$$\text{Gaussian}\left(\left(\frac{\sigma_y^2}{\sigma_z^2} Z + \frac{\sigma_x^2}{\sigma_z^2} \mu_x - \frac{\sigma_x^2}{\sigma_z^2} \mu_y\right), \frac{\sigma_x^2 \sigma_y^2}{\sigma_z^2}\right).$$

Proof: According to the definition of conditional distribution:

$$p(X | Z) = \frac{p(X, Z)}{p(Z)} = \frac{p(Z | X)p(X)}{p(Z)}. \quad (2.12)$$

Note that

$$p(Z | X) = p(X + Y | X) = p(Y) = p(Z - X). \quad (2.13)$$

Therefore, equation (2.12) becomes:

$$p(X | Z) = \frac{p(Z - X)p(X)}{p(Z)}$$

$$\begin{aligned}
&= \frac{\frac{1}{\sqrt{2\pi\sigma_y^2}} e^{-\frac{(y-\mu_y)^2}{2\sigma_y^2}} \frac{1}{\sqrt{2\pi\sigma_x^2}} e^{-\frac{(x-\mu_x)^2}{2\sigma_x^2}}}{\frac{1}{\sqrt{2\pi\sigma_z^2}} e^{-\frac{(z-\mu_z)^2}{2\sigma_z^2}}} \\
&= \frac{1}{\sqrt{2\pi \frac{\sigma_x^2 \sigma_y^2}{\sigma_z^2}}} e^{-\frac{[x - (\frac{\sigma_x^2}{\sigma_z^2} Z + \frac{\sigma_y^2}{\sigma_z^2} \mu_x - \frac{\sigma_x^2}{\sigma_z^2} \mu_y)]^2}{2(\frac{\sigma_x^2 \sigma_y^2}{\sigma_z^2})}} \\
&\sim \text{Gaussian}((\frac{\sigma_x^2}{\sigma_z^2} Z + \frac{\sigma_y^2}{\sigma_z^2} \mu_x - \frac{\sigma_x^2}{\sigma_z^2} \mu_y), \frac{\sigma_x^2 \sigma_y^2}{\sigma_z^2}).
\end{aligned}$$

□

Because the primary and scatter radiation of each pixel given B is independent of those of other pixels, $d_k^{(n)} = E[d_k | Y, B^{(n)}] = E[d_k | y_k = d_k + s_k, B^{(n)}]$. Consider random variables in Theorem 2.1 to be $X=d_k$, $Y=s_k$ and $Z=y_k$, therefore,

$$d_k^{(n)} = (\sigma_{k1}^2 y_k + \sigma_{k2}^2 b_k^{(n)} - \sigma_{k1}^2 (B^{(n)} ** P)_k) / (\sigma_{k1}^2 + \sigma_{k2}^2). \quad (2.14)$$

Then equation (2.11) combines with equation (2.14) to give the following updating equation:

$$b_k^{(n+1)} = b_k^{(n)} + W_k \cdot [y_k - (b_k^{(n)} + (B^{(n)} ** P)_k)], \quad (2.15)$$

where

$$W_k = \sigma_{k1}^2 / (\sigma_{k1}^2 + \sigma_{k2}^2). \quad (2.16)$$

2.4 Incorporation of Gibbs Prior

MLEM is known to have adverse effect on high frequency image noise. To overcome this, some constraints can be put on the noise level within the estimated B , or in other words, the prior information about B is provided. By Bayes's Rule,

$$p(B|Y) \propto p(Y|B)p(B), \quad (2.17)$$

where $p(B)$ is the prior joint distribution of $B=\{b_i; i=1,\dots,N\}$, $p(Y|B)$ is equal to the likelihood of B , and $p(B|Y)$ is the posterior joint distribution of B given measured pixel values $Y=\{y_i; i=1,\dots,N\}$.

We assume B is a Markov random process; it therefore follows a Gibbs distribution:

$$p(B) = \frac{1}{K} e^{-U(B)/\beta}, \quad (2.18)$$

where K is a normalizing factor which is independent of B , $U(B)$ is the energy function, and β is a free parameter adjusting the relative weight of this prior on the maximum *a posteriori* (MAP) estimator of B . When β is approaching infinity, the MAP of B approaches MLE of B .

The energy function is the sum of the potential function, i.e.,

$$U(B) = \sum_{c \in C} V_c(B), \quad (2.19)$$

where C is the set comprised of all cliques in the image. One clique is defined as a set of pixels where each one is a neighbor of all the others in the same clique. In the thesis, the Gibbs prior is defined over a 2nd-order neighborhood system (for each

pixel its north, south, east, west neighboring pixels plus its four diagonal neighboring pixels) with each clique comprising of two neighboring pixels. There are many forms of the potential function $V_c(b)$. The one we pick up is adaptive to discontinuity [35-37]:

$$V(\{b_i : b_j\}) = \frac{(b_i - b_j)^2}{\delta_c^2 + (b_i - b_j)^2}, \quad (2.20)$$

where i and j are the neighboring pixels within the clique $i \sim j$. The b_i and b_j represent their intensities. δ_c is an adjustable parameter to regulate the cut-off frequency of the noise in the image.

2.5 Image Acquisition

A Siemens prototype digital mammography system (Mammomat Novation^{DR}) with 70 μm isotropic resolution was used for image acquisition. Uniform breast phantoms (CIRS, Inc., Norfolk, VA) were imaged with the x-ray beam generated by 28kVp and Mo/Mo target/filter combination. The phantoms are radiographically equivalent to a compressed breast of 4cm in thickness and 50% in glandular tissue density. At the center of the phantom there is a square dent, which mimics a high-contrast lesion in the digital mammography images. The images used in this thesis were acquired without an anti-scatter grid. Some of them have a beam stop (i.e., lead discs with 3mm diameter) array superimposed on the breast phantoms. The beam stop method is a standard technique to measure the scatter radiation. Because lead discs absorb all

the primary radiation, only scatter radiation can arrive behind them. Figure 2.2 shows one such image.

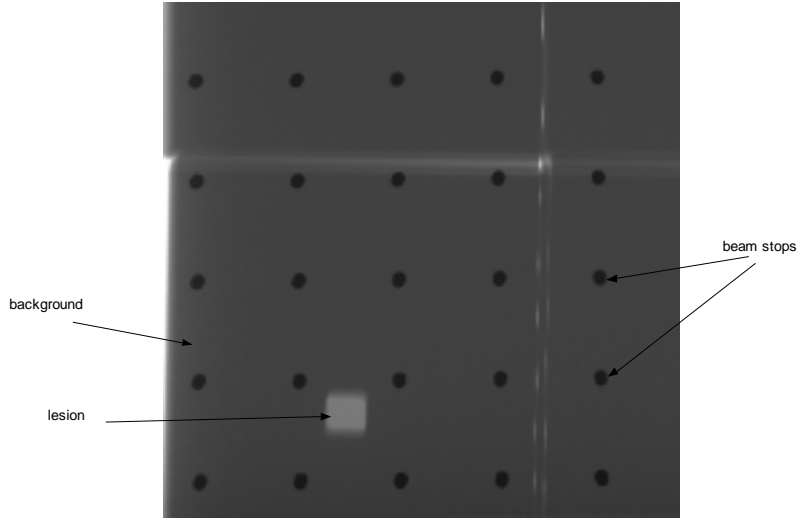


Figure 2.2: A sample breast phantom image taken with the beam stop array superimposed. The bright square mimics a high density lesion, based on which the contrast and CNR values are obtained.

The image can then be fed into the algorithms for processing. The effect of processing is evaluated through various metrics, which will be discussed in the following subsection.

2.6 Image Analysis Metrics

The primary purpose of the algorithms is to estimate the expectation of primary radiation. Its effect is measured by the residual scatter fraction (RSF). At the same

time, it is desirable that the contrast-to-noise ratio (CNR) will be constrained or even improved after image processing. In addition, the effect of the algorithms on spatial resolution of the image has to be carefully monitored. In the following, we will give the definition of each of these metrics and how they are measured in this thesis.

2.6.1 Residual Scatter Fraction

Scatter fraction (SF) is defined as the ratio of the scatter radiation to the total radiation. Residual scatter fraction (RSF) is a quantity used to indicate how much of the scatter radiation remains after applying the scatter compensation algorithm.

For the given imaging technique, two sets of images of the phantom were obtained. One is taken without a beam stop array, and the other is taken with the beam stop array. The signals behind beam stops (lead discs) are the scatter radiation. The total radiation, which is the sum of primary radiation and the scatter radiation, will reach the region without the beam stops. Thus the measured primary radiation (P_{measured}) is calculated by subtracting the mean radiation of a region-of-interest (ROI) behind a beam stop from the mean of the same ROI location without a beam stop. In the image processed for scatter compensation, the mean of total radiation (T) in the same ROI location ($T_{\text{estimated}}$) is the sum of the residual scatter radiation and the primary radiation. Then

$$RSF = \frac{T_{\text{estimated}} - P_{\text{measured}}}{T_{\text{estimated}}}. \quad (2.21)$$

2.6.2 Contrast, Noise and CNR

The contrast is defined as the ratio of the difference between the mean value of the lesion (T_{lesion}) and that of the background ($T_{\text{background}}$) to the mean of the background.

That is,

$$\text{Contrast} = \frac{T_{\text{lesion}} - T_{\text{background}}}{T_{\text{background}}}. \quad (2.22)$$

The noise is derived by dividing the standard deviation ($STD_{\text{background}}$) to the mean ($T_{\text{background}}$) of the background:

$$\text{Noise} = \frac{STD_{\text{background}}}{T_{\text{background}}}. \quad (2.23)$$

Contrast-to-noise ratio is the ratio of the contrast to the noise. i.e.,

$$\text{CNR} = \frac{\text{Contrast}}{\text{Noise}} = \frac{T_{\text{lesion}} - T_{\text{background}}}{STD_{\text{background}}}. \quad (2.24)$$

2.6.3 Resolution

Due to the nonlinearity of the algorithm, the metric like modulation transfer function (MTF) which is designed for a linear system can not be used here. Instead, a test bar comprised of alternating bright and dark lines with size corresponding to Nyquist frequency are embedded in the phantom image.

The contrast improvement factor (CIF), defined as the ratio of the contrast after image processing to the initial contrast, is obtained for the test bar with various initial

contrast. If CIF is not less than 1, no resolution is lost. Otherwise, resolution is degraded. The minimal initial contrast that the test bar can take on with CIF no less than 1 is recorded as an indication of the effect of the image processing on resolution.

Chapter 3

Results and Discussion

3.1 Normality Check of the Data

In our new model, primary, scatter and total radiations of each pixel in the projection mammography images are assumed to follow Gaussian distributions. To check whether Gaussian distribution is a good approximation to the real data, we analyze a uniform ROI outside of a beam stop (ROI1) and a uniform ROI behind a beam stop (ROI2) in an image acquired without an anti-scatter grid.

ROI1 is a square region with 201x201 pixels, and its histogram is plotted in Figure 3.1. Visually, it follows approximately a Gaussian distribution. For further evaluation, the empirical quantile-quantile plot of the data with respect to a standard Gaussian distribution is drawn in Figure 3.2. The quantile of the data has a nice linear relationship with the quantile of the standard Gaussian distribution, indicating that the total radiation can be well represented by a Gaussian distribution.

As stated before, the exposure of the area behind a beam stop is due to the scattered radiation from the neighboring regions. Figure 3.3 shows the profile of radiation along a line through the center of a beam stop. It has a nice flat profile for the scatter radiation. The circular ROI2 is selected which has a total number of 441 pixels. Its histogram and quantile-quantile plot with respect to the standard Gaussian

distribution are shown in Figure 3.4 and Figure 3.5 respectively. Figure 3.5 shows that scatter radiation is also approximately Gaussian distribution.

It is obvious that both total radiation shown in Figure 3.1 and scatter radiation shown in Figure 3.4 can not be directly modeled as Poisson distributions, since 1) the radiation does not take on discrete integer values only; and 2) the variance is much smaller than the mean, whereas a Poisson distribution has an equal variance and mean. Therefore, from the modeling perspective, the Poisson noise model (shown in block (2.2)) is problematic especially when a computation method other than EM algorithm is used. Luckily, if the model is modified by adding a latent data, then the iterative equation (equation (2.3)) derived from EM algorithm can be approximately true under certain assumptions.

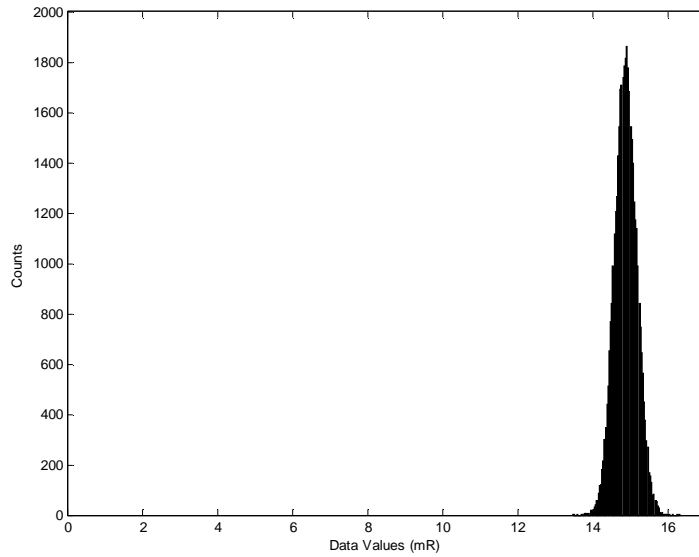


Figure 3.1: The histogram of data from a uniform region-of-interest with total of 201x201 pixels in an image acquired without an anti-scatter grid. The data is seen to be approximately Gaussian distribution.

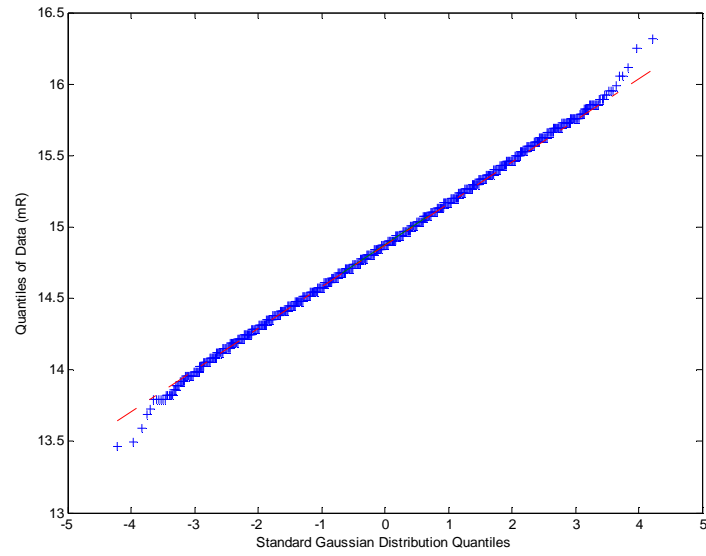


Figure 3.2: The quantile-quantile plot of the same data as in Figure 3.1 with respect to the standard Gaussian distribution with mean of 0 and standard deviation of 1. The data fits well with the Gaussian distribution.

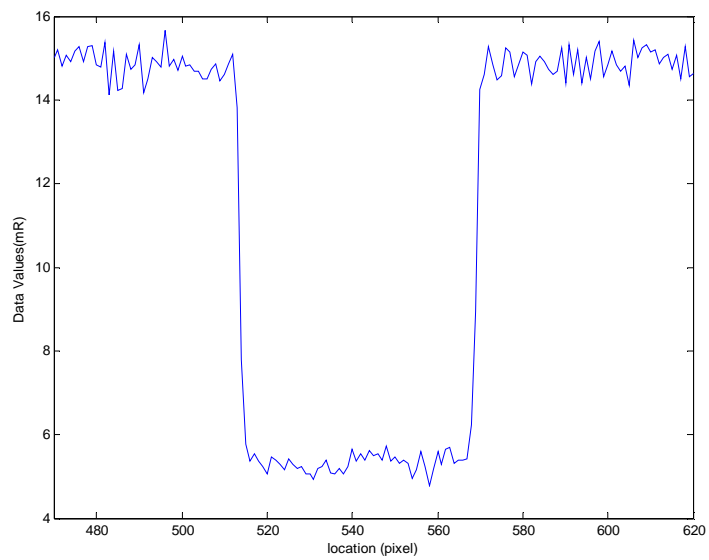


Figure 3.3: One-dimensional profile through the center of a beam stop (or lead disc).

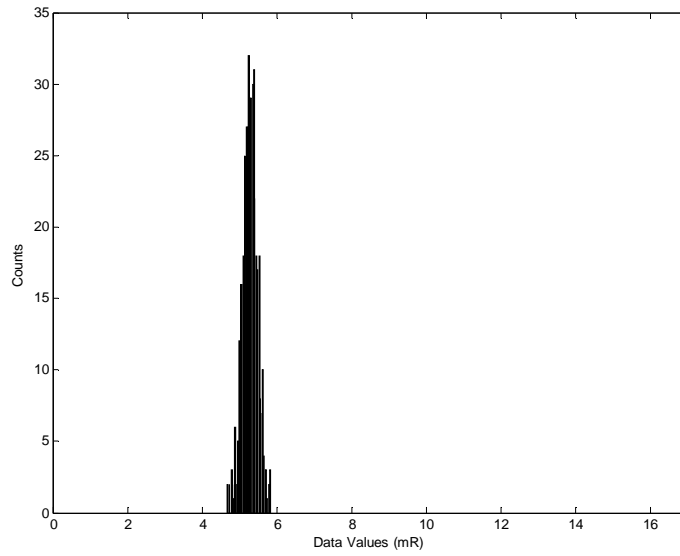


Figure 3.4: The histogram of data from a circular region-of-interest with total of 441 pixels behind a beam stop in an image acquired without an anti-scatter grid. The data is seen to be approximately Gaussian distribution.

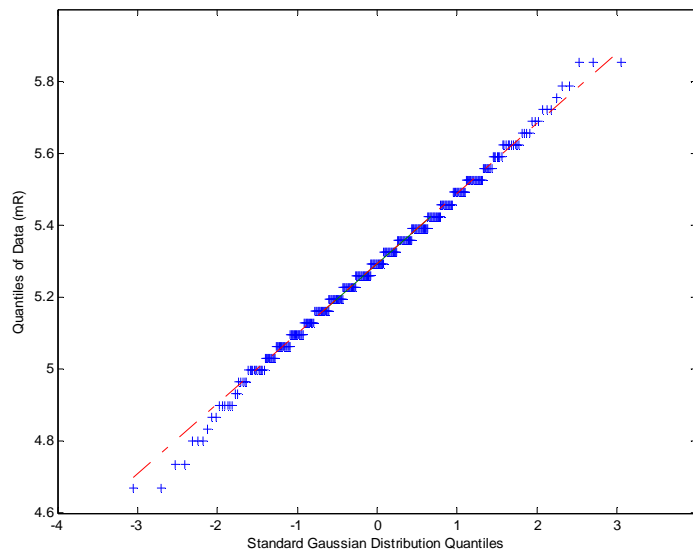


Figure 3.5: The quantile-quantile plot of the same data as in Figure3.4 with respect to the standard Gaussian distribution with mean of 0 and standard deviation of 1.

Except an outlier (data value is about 1.7mR), the rest data fits well with the Gaussian distribution.

3.2 Latent Data Augmentation Scheme for Poisson Model

Assume the exposure or radiation is intrinsically proportional to the number of photons that produce the radiation through a constant C (E), which is dependent on the energies of photons E . For d_i , s_i and y_i , the corresponding number of photons are nd_i , ns_i , and ny_i . The expected number of photons for nd_i is nb_i . The following model is valid:

$$\left. \begin{aligned} nd_i &| NB \sim \text{Poisson}(nb_i) \\ ns_i &| NB \sim \text{Poisson}((B ** P)_i) \\ ny_i &= nd_i + ns_i | NB \sim \text{Poisson}(nb_i + (NB ** P)_i) \end{aligned} \right\} \quad (3.1)$$

The updating equation for nb_i is the same as equation (2.3):

$$nb_k^{(n+1)} = nb_k^{(n)} \cdot \frac{ny_k}{nb_k^{(n)} + (NB^{(n)} ** P)_k} \quad (3.2)$$

If by simplification, assume a single energy independent conversion constant C instead of a set of $C(E)$ exists, then

$$\begin{aligned} b_k &= E(d_k) = C \cdot E(nd_k) = C \cdot nb_k \\ y_k &= C \cdot ny_k \end{aligned} \quad (3.3)$$

And then,

$$b_k^{(n+1)} = b_k^{(n)} \cdot \frac{y_k}{b_k^{(n)} + (B^{(n)} ** P)_k} \quad (3.4)$$

which is the same updating equation for b_k as equation (2.3). In other words, as long

as a single conversion constant rather than a set of energy dependent conversion constants $C(E)$ exists between the radiation and the number of photons, The equation (2.3) or (3.3) derived from EM algorithm is scale-invariant regardless of the value of latent data C .

3.3 Comparison between the Poisson and Gaussian Models

Gaussian noise model is sounder than Poisson noise model for the direct modeling of radiations. Poisson model won't give an accurate answer if computation methods which rely heavily on the accuracy of the model such as Gibbs sampling are adopted. However, when EM algorithm is used, the iterating equation obtained based on Poisson assumption can roughly be used to update the expectation of primary radiation. This is based on a simplification that a single conversion factor is valid for all radiation levels, which is not true in reality. By contrast, Gaussian noise model allows for the different conversion factors for different energies.

For the uniform breast phantom, empirical value of W_i ($i=1,\dots,N$) in the Gaussian model as shown in equation (2.16) is 0.45. The empirical optimized scatter kernel P has FWHM=80pixels (i.e., 5.6mm) and $M=0.52$. The images are processed to obtain the MLE estimates from both models. Also the MAP estimates are obtained from both models using the same Gibbs prior with delta of 0.10.

As a convention, in all the figures shown hereafter, the values for iteration 0 are the values measured on the original image without any processing.

Figure 3.6 shows the plots of RSF of MLE and MAP estimates from both models as a function of iteration number. All estimators successfully reduce the scatter radiation in the processed image such that RSF drops with iteration. In addition, they all asymptotically converge to the same value of 0.019 from the original scatter fraction of 0.354. Note that estimators based on Poisson noise model have a slightly faster convergence rate than those based on Gaussian noise model. For example, at iteration 2, the RSF of estimators from Poisson model already drops to 0.019, whereas that from Gaussian model is 0.047.

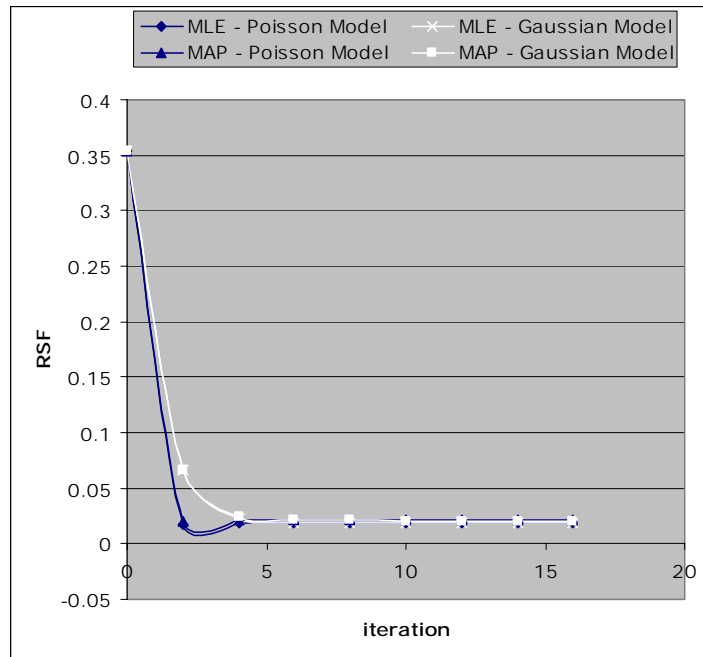


Figure 3.6: RSF vs. iteration plots for MLE and MAP estimator of b from both the Poisson noise model and the Gaussian noise model. The magnitude of scatter kernel is 0.52, which is same as the measured scatter-to-primary ratio (SPR). Therefore, RSF all drops close to zero, meaning almost complete scatter compensation.

Figure 3.7 to Figure 3.9 illustrate how noise, contrast and CNR individually

change with iteration numbers. Let's look at Figure 3.7 first. At iteration 16, the MLE estimators of both Poisson model and Gaussian model increase the noise from the original 0.021 to 0.031, which corresponds to a 47.6% of increase. The MAP estimator from Poisson model keeps the noise at a roughly same level as the original image, whereas the MAP estimator from Gaussian model decreases the noise by 5.6%.

Figure 3.8 show that all four estimators increase the contrast similarly. At iteration 16, they all increase the contrast by 26.8%.

As shown in Figure 3.9, the initial CNR of the lesion is 47.28. After processing by both MLE methods, the CNR of the lesion drops to 39.13, which is equivalent to a 17.2% change. By contrast, the MAP estimators from Poisson and Gaussian models successfully increase CNR by 18.7% and 34.2% respectively.

Table 3.1 shows the resolution results for the MAP estimates from the Poisson noise model and the Gaussian noise model. Both models can retain resolution for initial contrast greater than 2%. Poisson model retains the resolution slightly better than Gaussian model. It is not shown in Table 3.1 that MLE estimates from both models retain the resolution at all initial contrast levels.

In summary, both MLE and MAP estimators work equally well in reducing the scatter radiation, while MAP estimators works better than their MLE counterparts in improving or constraining CNR without general loss of resolution. MAP estimator based on Gaussian model has a better performance in improving or constraining CNR than the MAP estimator based on Poisson model.

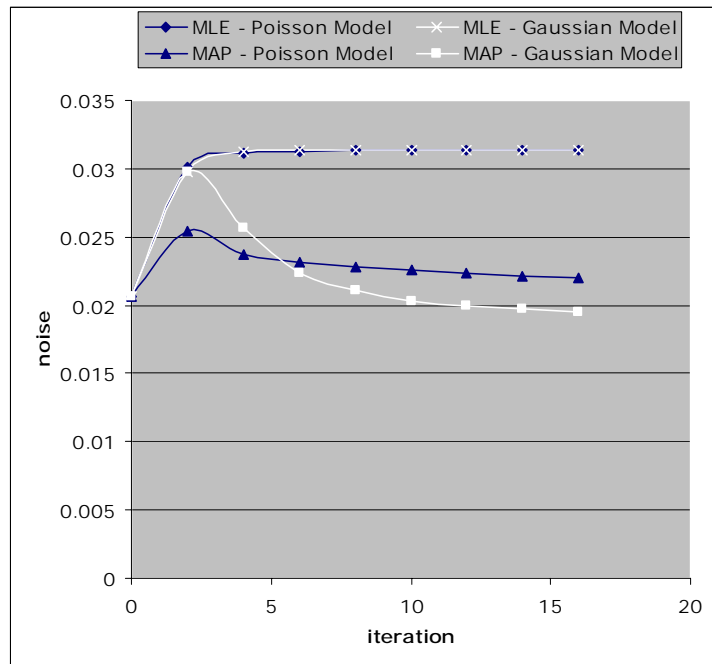


Figure 3.7: The noise vs. iteration plots for MLE and MAP estimator of b from both the Poisson noise model and the Gaussian noise model.

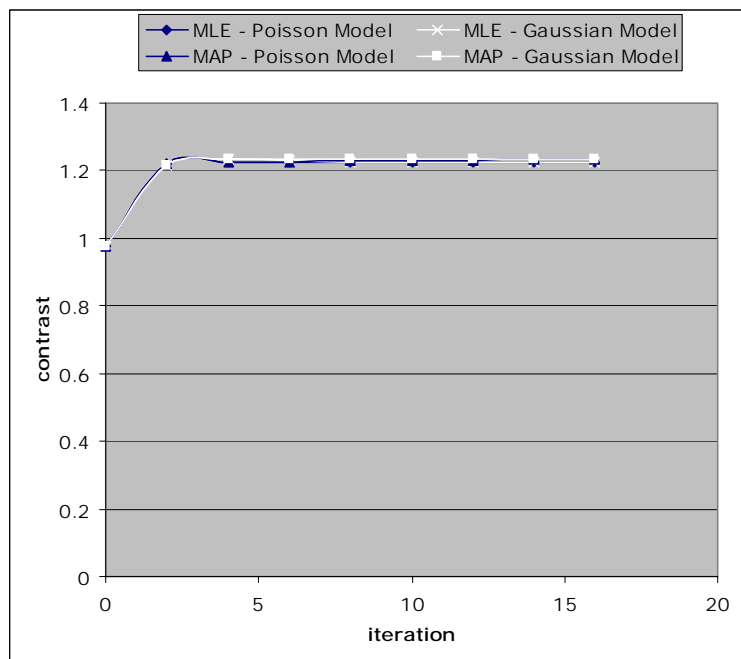


Figure 3.8: The contrast noise vs. iteration plots for MLE and MAP estimator of b from both the Poisson noise model and the Gaussian noise model.

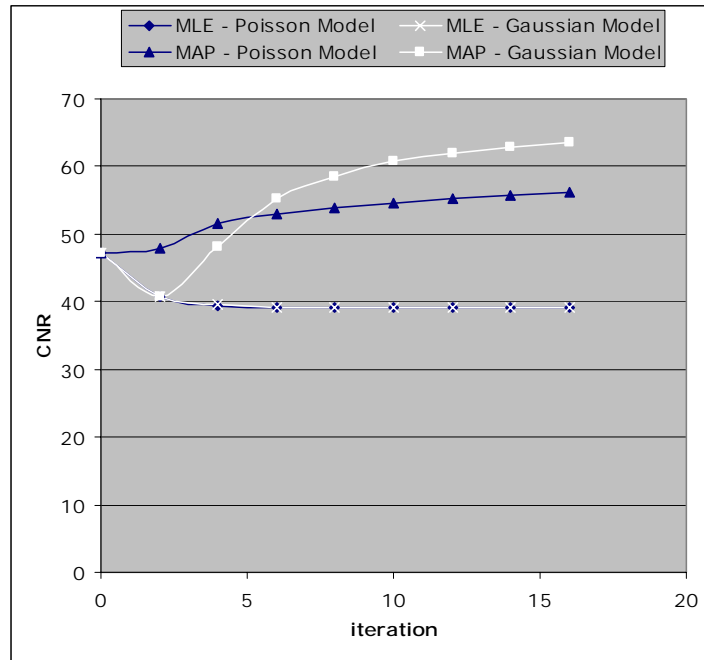


Figure 3.9: The CNR vs. iteration plots for MLE and MAP estimator of b from both the Poisson noise model and the Gaussian noise model.

	Poisson Model	Gaussian Model
Minimum initial contrast that is retainable during processing	1.8%	2.0%

Table 3.1: The resolution results for Poisson model and Gaussian model. The square wave function with Nyquist frequency is used as the test object. For various initial contrasts, the corresponding contrast-improvement-factor (CIF) is computed at iteration 16. CIF no less than 1 is used as the criterion for retaining the spatial resolution. What is reported here is the minimal initial contrast that has CIF no less

than 1.

3.4 Further Evaluation of Gaussian Noise Model

3.3.1 Effect of the Magnitude of the Scatter Kernel

The Magnitude of the Scatter Kernel M , which is the same as the area under the curve, is used to model the scatter-to-primary ratio (SPR). Using the specified technique, the measured SPR for the phantom is 0.52. As is shown in Figure 3.10, when M is specified as 0.52, the RSF drops rapidly from the initial value to a value close to zero, meaning a satisfactory scatter compensation effect. When M is less than 0.52, the scatter radiation is partially compensated. Specifically, when M equals zero, no scatter compensation is made. When M is larger than 0.52, the scatter radiation is over-compensated, i.e., RSF is less than zero.

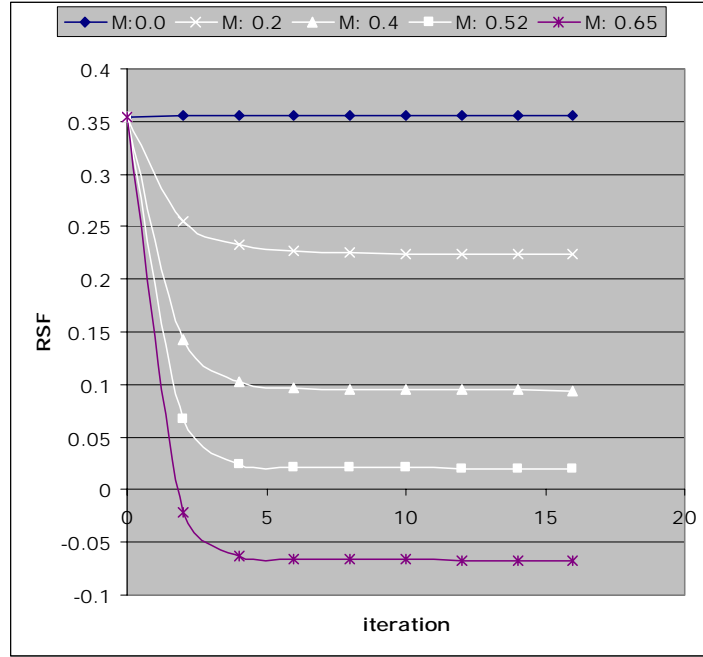


Figure 3.10: The RSF vs. iteration curves for the magnitude (M) of the scatter kernel ranging from 0.0 to 0.65. The measured SPR value using the beam stop technique is 0.52. M of 0.0 represents no scatter compensation. M of 0.20 and 0.40 represents partial scatter compensation. And M of 0.65 overcompensate the scatter radiation in the image.

Figure 3.11 -3.13 illustrate how different magnitude of the scatter kernel affects the noise, contrast and CNR respectively. Overall, these three metrics change monotonically with respect to the magnitude M . More specifically, when M gets larger, both the noise and the contrast become larger, while the CNR gets smaller.

For all the M values investigated, the CNR at iteration 16 is larger than the original value. When M is equal to 0, the CNR improves by as large as 74.7%; even for M of 0.65, CNR improves by 24.3%.

Table 3.2 gives the resolution results for the Gaussian model with various magnitude of scatter kernel. Note that for a magnitude of zero, there will always be

resolution loss. For the rest magnitude values, the resolution performances are similar.

If the scatter compensation is the major concern, then the magnitude should be chosen as close to the actual SPR value as possible. The image processed in this setting will improve or constrain CNR without general loss of resolution. If more noise reduction or more CNR improvement is desired, then a smaller magnitude can be selected, at the expense of partial scatter compensation. The magnitude of zero, however, is not a good choice because it reduces the noise and increases the CNR at the expense of all spatial resolution as well as no scatter compensation.

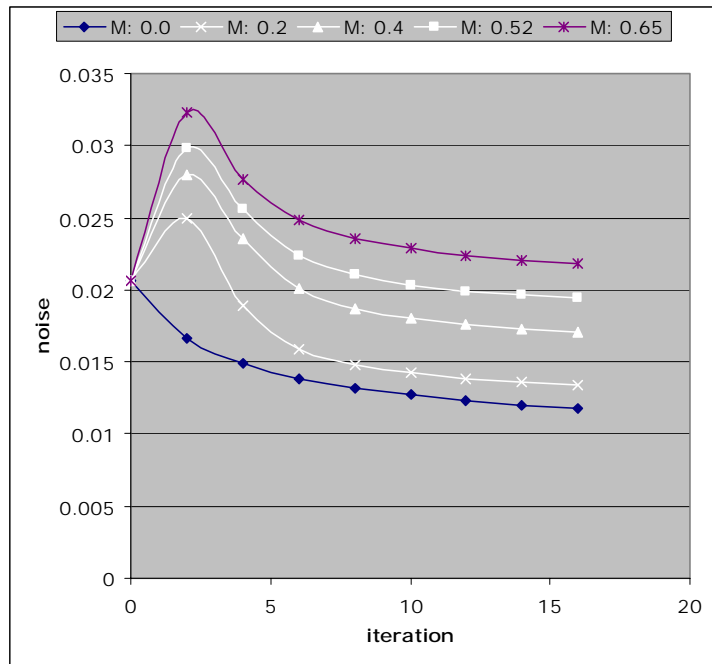


Figure 3.11: The noise vs. iteration curves for M ranging from 0.0 to 0.65. At each M level, the percentage noise reduces asymptotically. The smaller the M value is, the more is the percentage noise reduced from the initial value of 0.021.

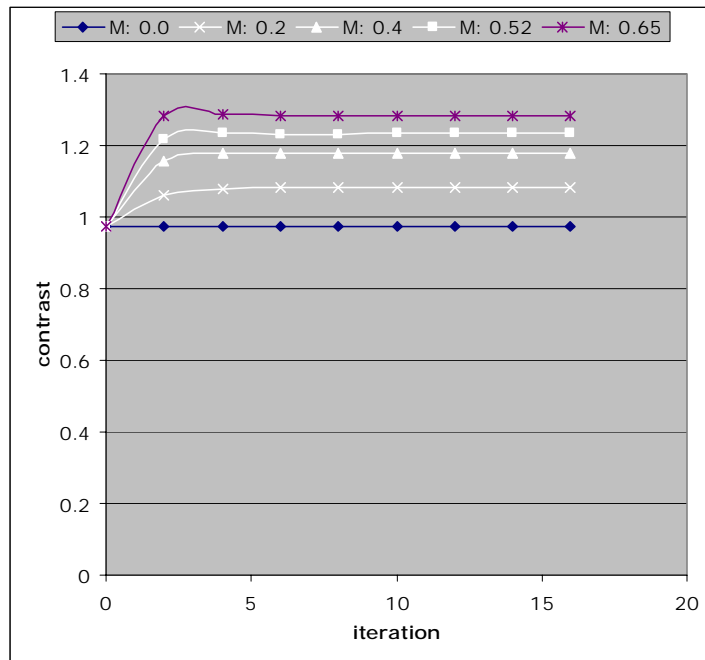


Figure 3.12: The contrast vs. iteration curves for M ranging from 0.0 to 0.65. At each magnitude level, the contrast increases asymptotically. The larger the magnitude is, the more is the contrast increased from the initial value of 0.97.

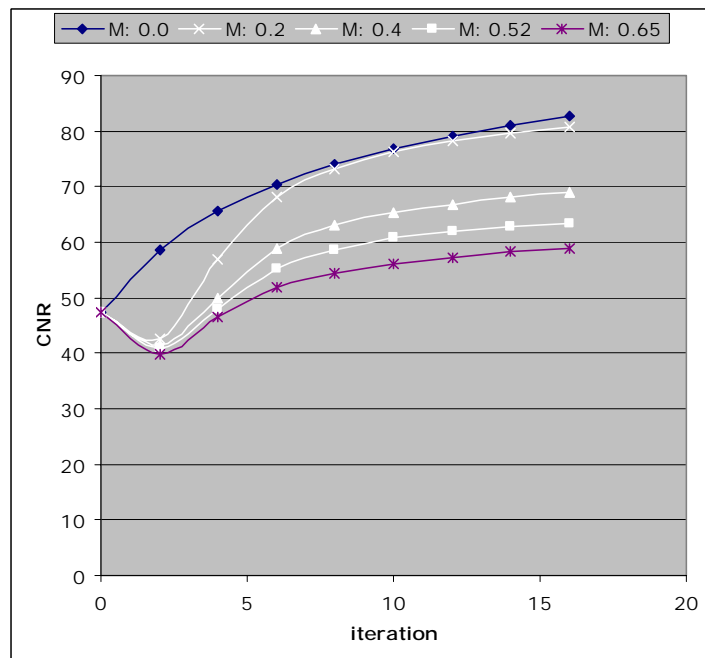


Figure 3.13: The CNR vs. iteration curves for M ranging from 0.0 to 0.65. At each magnitude level, the contrast increases asymptotically. The smaller the magnitude is, the more is the contrast increased.

Magnitude	0.0	0.2	0.4	0.52	0.65
Minimal initial contrast	---	2.7%	2.2%	2.0%	2.0%

Table 3.2: The resolution results for the Gaussian noise model with different magnitude of scatter kernel.

3.3.2 Effect of the Delta in the Gibbs Prior

As mentioned in the subsection 2.4, the delta (δ) in the potential function of the Gibbs prior can be considered as a factor controlling cut off frequency in the processed image. The results shown in the previous sections are for $\delta=0.10$. Now let's consider δ of 0.2 and 0.05 to see how plots for the image quality metrics change. As expected, different δ values do not change the RSF and the contrast plots, so their plots are not shown. Figure 3.14, Figure 3.15 and Table 3.3 give the noise, CNR plots and the resolution result for delta of 0.2. Figure 3.16, Figure 3.17 and Table 3.4 show the corresponding results for delta of 0.05. By comparing these results to Figure 3.7, Figure 3.9 and Table 3.1 for delta of 0.1, the trend emerges: the larger δ is, the more the image will be smoothed at the expense of slightly more resolution loss. It is understandable since more smoothed the final image is (i.e., less noise in the final image), more likely the details will lose. But still the final image retains a

reasonably good spatial resolution (for test bar of smallest possible size (corresponding to Nyquist frequency), all initial contrasts of 3% or larger is retained). When delta is 0.2, CNR in the MAP estimator based on the Gaussian model improves by as large as 120% without general loss of resolution.

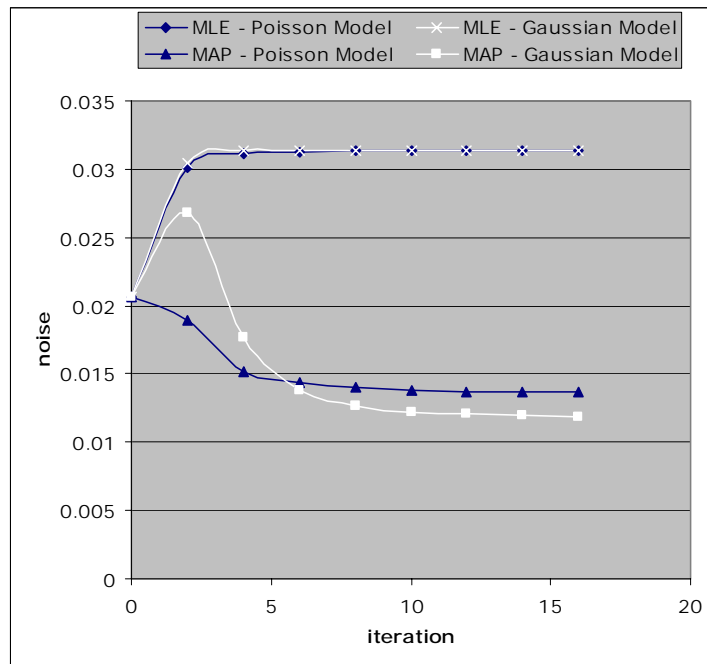


Figure 3.14: The noise vs. iteration plots for MLE and MAP estimators based on delta of 0.2. The MAP estimators decrease the noise more than their counterparts based on delta=0.1 as shown in Figure 3.6.

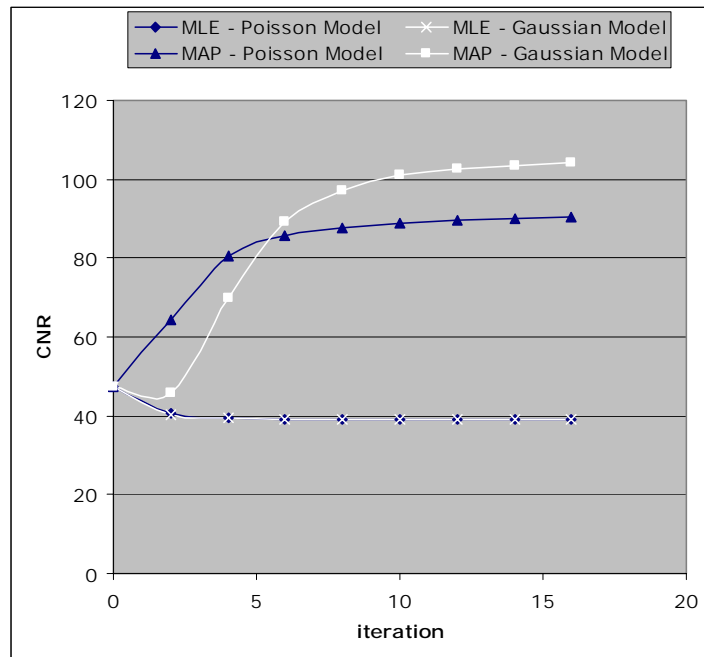


Figure 3.15: The CNR vs. iteration plots for MLE and MAP estimators based on delta of 0.2. The MAP estimators increase the CNR more than their counterparts based on delta=0.1 as shown in Figure 3.8. Also, the MAP estimator from Gaussian model improves CNR more than the one from Poisson model.

	Poisson Model	Gaussian Model
Minimum initial contrast that is retainable during processing	3.0%	3.1%

Table 3.3: The resolution results for Poisson model and Gaussian model when delta=0.2.

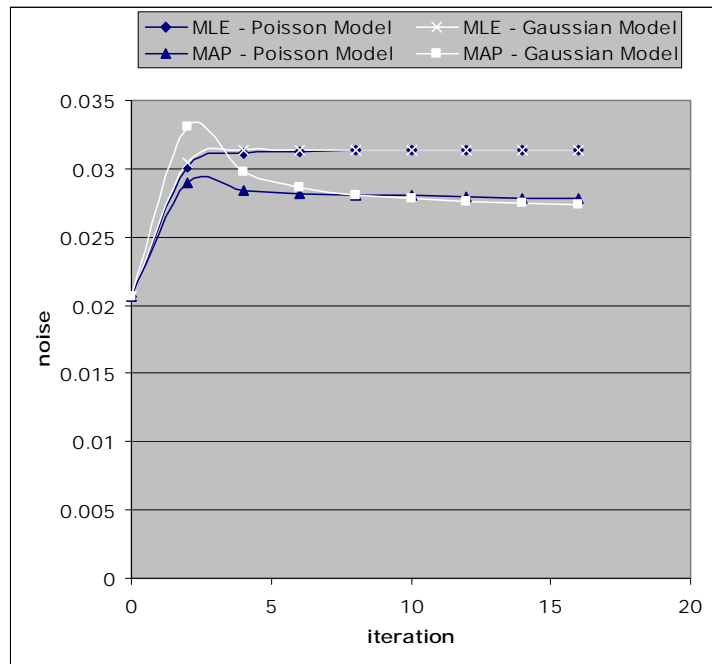


Figure 3.16: The noise vs. iteration plots for MLE and MAP estimators based on delta of 0.05. The MAP estimators decrease the noise less than their counterparts based on delta=0.1 as shown in Figure 3.6.

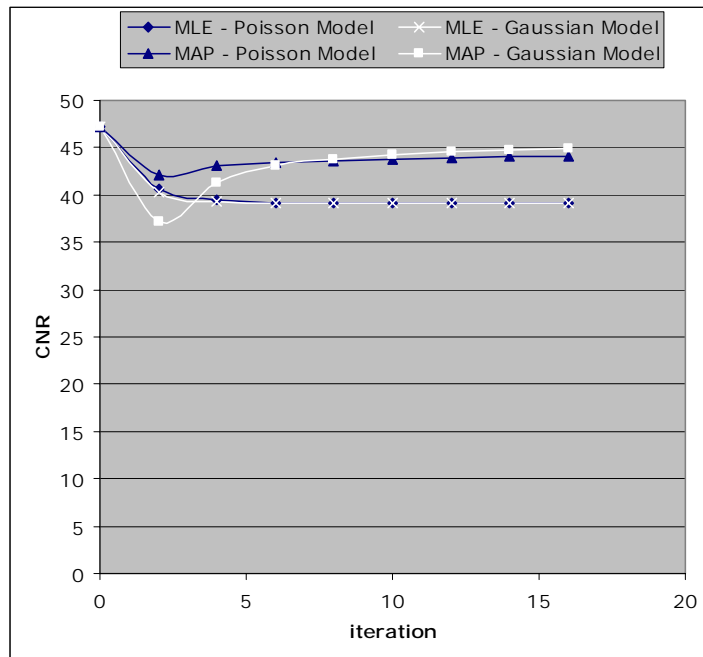


Figure 3.17: The CNR vs. iteration plots for MLE and MAP estimators based on delta of 0.05. In this case, the MAP estimators performs better than the MLE estimators in constraining CNR, but performs worse than their counterparts based on delta=0.1 as shown in Figure 3.8. But the MAP estimator from Gaussian model is still slightly better than the one from Poisson model.

	Poisson Model	Gaussian Model
Minimum initial contrast that is retainable during processing	1.2%	1.6%

Table 3.4: The resolution results for Poisson model and Gaussian model when delta=0.05.

Chapter 4

Conclusion

By checking the experimental data, it was found that the Poisson noise model for scatter compensation in the literature [26] can not account for the radiations (including the primary, scatter and total radiations) directly. It will lead to an erroneous result for the estimation of the expected values of primary radiation if a computation method like Gibbs sampling is used. Luckily, due to the scaling-invariant property of EM algorithm with an approximation that a single factor rather than a set of energy dependent ones exists between the conversion of radiation and the corresponding number of photon, the updating equation derived from the old model can still be useful.

The histograms of radiation data indicate that they might be modeled by a different distribution like Gaussian. The quantile-quantile plots of the data with respect to the standard Gaussian distribution show that Gaussian noise model can be reasonably assumed. The EM algorithm based on this new model is derived and implemented. A MAP algorithm by incorporating a Gibbs prior is also implemented for better CNR in the processed images.

The MLE and MAP estimators from the Gaussian noise model are compared with their counterparts based on the Poisson noise model. Results show that MAP estimators from both models have better CNR performance than MLE ones without a

significant loss of resolution. In addition, the MAP estimator from Gaussian model performs better than the one from Poisson model in CNR improvement.

Further evaluation of MAP estimators from Gaussian model shows that both the magnitude of the scatter kernel and the delta in the Gibbs prior can be used to adjust the noise and CNR level in the processed images. The delta in the Gibbs prior acts as a major tuner of CNR without affecting RSF, whereas the magnitude of the scatter kernel acts as a fine tuner of CNR. Changing the magnitude of the scatter kernel will also affect the scatter compensation level. There is a general tradeoff between the CNR improvement and resolution reservation. Fortunately, for the largest CNR improvement (2.2 times the original CNR), the resolution is still reasonably well reserved.

References

- [1] Encyclopedia Britannica, Breast Cancer. Encyclopedia Britannica, 2005.
- [2] ACS, American Cancer Society: Cancer Facts and Figures 2005. Atlanta, GA: American Cancer Society, 2005.
- [3] ML Giger, Computer-aided diagnosis in radiology. *Academic Radiology*, 9: 1-3, 2002.
- [4] CE Floyd Jr, JY Lo, and GD Tourassi, Cased-based reasoning computer algorithm that uses mammographic findings for breast biopsy decisions. *American Journal of Roentgenology*, 175: 1347-1352, 2000.
- [5] HP Chan, *et al*, Improvement in radiologists' detection of clustered microcalcifications on mammograms: The potential of computer-aided diagnosis. *Investigative Radiology*, 25: 1102-1110, 1990.
- [6] ED Pisano, C Gatsonis, E Hendrick, *et al*, Diagnostic performance of digital versus film mammography for breast-cancer screening. *New England Journal of Medicine*, 353 (17): 1773-1783, 2005.
- [7] P Skaane, A Skjennald, Young K, *et al*, Follow-up and final results of the Oslo I study comparing screen-film mammography and full-field digital mammography with soft-copy reading. *Acta Radiologica*, 46 (7): 679-689, 2005.
- [8] RSNA: Radiological Society of North America website: <http://www.rsna.org/rsna/media/pr2005/internet.cfm>
- [9] JT Dobbins III, DJ Godfrey, Digital x-ray tomosynthesis: current state of the art and clinical potential. *Physics in Medicine and Biology*, 48 (19): R65-R106, 2003.
- [10] Y Chen, JT Dobbins III, Impulse response analysis for several digital tomosynthesis mammography reconstruction algorithms. *Proceedings of SPIE Medical Imaging*, 5745, 2005.
- [11] JT Bushberg, JA Seibert, EM Leidholdt Jr, and JM Boone, The essential physics of medical imaging (2nd edition). Lippincott Williams and Wilkins, Philadelphia,

PA, 2002.

- [12] S Moore, *et al*, Evaluation of scatter compensation methods by their effects on parameter estimation from SPECT projections. *Medical Physics*, 28(2): 278-287, 2001.
- [13] H Zaidi, Reconstruction-based estimation of the scatter component in Positron Emission Tomography. *Ann Nucl Med Sci*, 14: 161-172, 2001.
- [14] L Niklason, J Sorenson, and J Nelson, Scattered radiation in chest radiography. *Medical Physics*, 8(5): 677-681, 1981.
- [15] AH Baydush, CE Floyd Jr, Improved image quality in digital mammography with image processing. *Medical Physics*, 27 (7): 1503-1508, 2000.
- [16] HP Chan, KL Lam, and Y Wu, Studies of performance of antiscatter grids in digital radiography: Effect on signal-to-noise ratio. *Medical Physics*, 17(4): 655-664, 1990.
- [17] GT Barnes, H Cleare, and IA Brezovich, Reduction of scatter in diagnostic radiology by means of a scanning multiple slit assembly. *Radiology*, 120: 691-694, 1976.
- [18] U Neitzel, Grids or air gaps for scatter reduction in digital radiography: a model calculation. *Medical Physics*, 19(2): 475-481, 1992.
- [19] JY Lo, CE Floyd Jr, and CE Ravin, Scatter compensation in chest radiography with a single-exposure estimation-subtraction method. *Radiology*, 177(P): 172-173, 1990.
- [20] D Bailey and S Meikle, A convolution-subtraction scatter correction method for 3D PET. *Physics in Medicine and Biology*, 39: 411-424, 1994.
- [21] JA Seibert and JM Boone, X-ray scatter removal by deconvolution. *Medical Physics*, 15(4): 567-575, 1988.
- [22] JY Lo, CE Floyd Jr, and CE Ravin, Spatial-varying scatter compensation for portable chest radiographs using an artificial neural network, in Association of University Radiologists, Chicago, Ill. 1992.
- [23] CE Floyd Jr, *et al*, Scatter compensation for digital chest radiography using Maximum Likelihood Expectation Maximization. *Investigative Radiology*, 28(5): 427-433, 1993.

- [24] CE Floyd Jr, *et al*, Bayesian restoration of chest radiographs: Scatter compensation with improved signal to noise ratio. *Investigative Radiology*, **29**(10): 904-910, 1994.
- [25] AH Baydush, and CE Floyd Jr, Bayesian image estimation of digital chest radiography – interdependence of noise, resolution and scatter fraction. *Medical Physics*, **22** (8): 1255-1261, 1995.
- [26] AH Baydush, JE Bowsher, JK Laading, *et al*, Improved Bayesian image estimation for digital chest radiography. *Medical Physics*, **24** (4): 539-545, 1997.
- [27] CE Floyd Jr, *et al*, Measurement of scatter fractions in clinical bedside radiography. *Radiology*, **183**: 857-861, 1992.
- [28] CE Floyd Jr, *et al*, Posterior beam stop method for scatter fraction measurement in digital radiography. *Investigative Radiology*, **27**: 119-123, 1992.
- [29] CE Floyd Jr, *et al*, Deconvolution of compton scatter in SPECT. *Journal of Nuclear Medicine*, **26**:403-408, 1985.
- [30] CE Floyd Jr, *et al*, Scatter compensation in digital chest radiography by fourier deconvolution. *Investigative Radiology*, **24**: 30-33, 1989.
- [31] B Axelsson, P Msaki and A Israelsson, Subtraction of compton-scattered photons in single-photon emission computerized tomography. *The Journal of Nuclear Medicine*, **25**:490-494, 1984.
- [32] JM Boone, BA Arnold, and JA Seibert, Characterization of the point spread function and modulation transfer function of scattered radiation using a digital imaging system. *Medical Physics*, **13**: 254-256, 1986.
- [33] CE Floyd Jr, RJ Jaszczak, CC Harris, *et al*, Energy and spatial-distribution of multiple order Compton scatter in SPECT – a monte carlo investigation. *Physics in Medicine and Biology*, **29** (10): 1217-1230, 1984.
- [34] HP Chan and Kunio Doi, Physics characteristics of scattered radiation in diagnostic radiology: Monte Carlo simulation studies. *Medical Physics*, **12**:152-165, 1985.
- [35] SZ Li, Discontinuity-adaptive MRF prior and robust statistics: A comparative

- study. *Image and Vision Computing*, 13 (4): 227-233, 1995.
- [36] SZ Li, On discontinuity-adaptive smoothness priors in computer vision. *IEEE Transactions on Pattern Analysis and Machine Intelligence*, 17(6):576-586, 1995.
- [37] DS Lalush and BMW Tsui, Simulation evaluation of Gibbs prior distributions for use in Maximum a posteriori SPECT reconstruction. *IEEE Transactions on Medical Imaging*, 11:267-275, 1992.